Monthly Notices
of the
ROYAL ASTRONOMICAL SOCIETY

MNRAS **469,** S427–S442 (2017)
Advance Access publication 2017 July 27

doi:10.1093/mnras/stx1912

Ion composition at comet 67P near perihelion: *Rosetta* observations and model-based interpretation

K. L. Heritier,[1⋆] K. Altwegg,[2] H. Balsiger,[2] J.-J. Berthelier,[3] A. Beth,[1] A. Bieler,[2] N. Biver,[4] U. Calmonte,[2] M. R. Combi,[5] J. De Keyser,[6] A. I. Eriksson,[7] B. Fiethe,[8] N. Fougere,[5] S. A. Fuselier,[9,10] M. Galand,[1] S. Gasc,[2] T. I. Gombosi,[5] K. C. Hansen,[5] M. Hassig,[2,9] E. Kopp,[2] E. Odelstad,[7] M. Rubin,[2] C.-Y. Tzou,[2] E. Vigren[7] and V. Vuitton[11]

[1]*Department of Physics, Imperial College London, Prince Consort Road, London SW7 2AZ, UK*
[2]*Physikalisches Institut, University of Bern, Sidlerstrasse 5, CH-3012 Bern, Switzerland*
[3]*LATMOS/IPSL-CNRS-UPMC-UVSQ, Saint-Maur, F-94100 Saint-Maur, France*
[4]*LESIA, Observatoire de Paris, PSL Research University, CNRS, Sorbonne Universités, UPMC Univ. Paris 06, Univ. Paris Diderot, Sorbonne Paris Cité, 5 place Jules Janssen, F-92195 Meudon, France*
[5]*Department of Atmospheric, Oceanic and Space Sciences, University of Michigan, Ann Arbor, MI 48109, USA*
[6]*BIRA-IASB, Royal Belgian Institute for Space Aeronomy, Ringlaan 3, B-1180 Brussels, Belgium*
[7]*Swedish Institute of Space Physics, Ångström Laboratory, Lägerhyddsvägen 1, E-751 24 Uppsala, Sweden*
[8]*Institute of Computer and Network Engineering (IDA), TU Braunschweig, D-38106 Braunschweig, Germany*
[9]*Southwest Research Institute, PO Drawer 28510, San Antonio, TX 78228, USA*
[10]*University of Texas at San Antonio, San Antonio, TX 78249, USA*
[11]*Université Grenoble Alpes, CNRS, IPAG, F-38000 Grenoble, France*

Accepted 2017 July 25. Received 2017 June 28; in original form 2017 March 31

ABSTRACT

We present the ion composition in the coma of comet 67P with newly detected ion species over the 28–37 u mass range, probed by *Rosetta* Orbiter Spectrometer for Ion and Neutral Analysis (ROSINA)/Double Focusing Mass Spectrometer (DFMS). In summer 2015, the nucleus reached its highest outgassing rate and ion-neutral reactions started to take place at low cometocentric distances. Minor neutrals can efficiently capture protons from the ion population, making the protonated version of these neutrals a major ion species. So far, only NH_4^+ has been reported at comet 67P. However, there are additional neutral species with proton affinities higher than that of water (besides NH_3) that have been detected in the coma of comet 67P: CH_3OH, HCN, H_2CO and H_2S. Their protonated versions have all been detected. Statistics showing the number of detections with respect to the number of scans are presented. The effect of the negative spacecraft potential probed by the *Rosetta* Plasma Consortium/LAngmuir Probe on ion detection is assessed. An ionospheric model has been developed to assess the different ion density profiles and compare them to the ROSINA/DFMS measurements. It is also used to interpret the ROSINA/DFMS observations when different ion species have similar masses, and their respective densities are not high enough to disentangle them using the ROSINA/DFMS high-resolution mode. The different ion species that have been reported in the coma of 67P are summarized and compared with the ions detected at comet 1P/Halley during the *Giotto* mission.

Key words: plasmas – methods: data analysis – Sun: UV radiation – comets: individual: 67P.

1 INTRODUCTION

The *Rosetta* spacecraft encountered comet 67P/Churyumov-Gerasimenko (67P/C-G) in 2014 August. While other cometary missions around 21P/Giacobini-Zinner, 1P/Halley, 26P/Grigg-Skjellerup and 19P/Borelly were fly-bys, *Rosetta* is the first mission

⋆ E-mail: k.heritier15@imperial.ac.uk

to escort a comet and orbit it in order to study the evolution of its coma and its interaction with the space environment (Glassmeier et al. 2007a). As a comet gets close to the Sun, the volatiles in the nucleus sublimate, forming an extended coma that is partially ionized by photoionization, electron-impact ionization and charge-exchange with the solar wind (Cravens et al. 1987). The escort of comet 67P by *Rosetta* lasted for 2 yr and ended on 2016 September 30. During this period, the comet went from a low outgassing object at 3.6 au from the Sun, where *Rosetta* encountered it to an active comet near perihelion (1.24 au) on 2015 August 13 and went back to its quiet state, reaching 3.8 au from the Sun in September 2016. The data collected during this 2-yr escort period provided us with a unique opportunity to assess the evolution and variability over seasons, spatial locations and heliocentric distances. In this paper, we focus on the ionosphere of comet 67P during its most active phase, near perihelion from 2015 July to September. In a rarefied environment, the ion composition gives constraints on how much chemistry is taking place and how many collisional interactions cometary ions go through, from their creation to the end of the pick-up process by the solar wind.

The *Rosetta* Orbiter Spectrometer for Ion and Neutral Analysis (ROSINA; Balsiger et al. 2007) includes the COmet Pressure Sensor (COPS) that measured the total neutral number densities and a Double Focusing Mass Spectrometer (DFMS), which measured the relative volume mixing ratios of the different neutral and ion species. The ionospheric population is only a ten thousandth of the total population with about 1100 cm^{-3} for the ions (Eriksson et al. 2017) versus 10^7 cm^{-3} for the neutrals (Fougere et al. 2016a) near perihelion. Ions are influenced by the local magnetic field and partially driven out of DFMS field of view (Fuselier et al. 2015). They are also influenced by the spacecraft potential, probed in real time by *Rosetta* Plasma Consortium (RPC)/LAngmuir Probe(LAP; Eriksson et al. 2007). Its voltage is negative during most of the mission (Odelstad et al. 2015; Eriksson et al. 2017) and can, on the top of the acceleration through the solar wind motional electric field, drive the ions out of DFMS energy acceptance window (Schläppi 2011). Because of these reasons, volume mixing ratios are more reliable for neutral than ion species at our current level of data analysis.

At perihelion (1.24 au), comet 67P reached an outgassing rate of about 10^{28} s^{-1} (Hansen et al. 2016). It is higher than the 4–8 $\times$ 10^{27} s^{-1} originally predicted by Hanner et al. (1985), Benna & Mahaffy (2006), Hansen et al. (2007), Lamy et al. (2007) and Tenishev, Combi & Davidsson (2008). By comparison, the spacecraft *Giotto* probed an outgassing rate of 7 $\times$ 10^{29} s^{-1} for 1P/Halley (Reinhard 1986) and 7.2 $\times$ 10^{27} s^{-1} for 26P/Grigg-Skjellerup (Flammer & Mendis 1993). Understanding the neutral population is crucial to characterize the ionospheric population. The ROSINA/DFMS instrument detected many volatile species in 67P (Hässig et al. 2015; Le Roy et al. 2015). The main ones are H_2O, CO_2 and CO. High proton affinity (HPA) neutrals in small quantities (<1 per cent volume mixing ratios), such as NH_3, HCN, H_2S and CH_3OH, were also detected (see Section 3.1 and Beth et al. 2016). Molecular oxygen was unexpected and contributes to about 1–10 per cent (depending on the period considered) of the total composition (Bieler et al. 2015). At Halley, the neutral and ion compositions were derived from measurements of the Neutral Mass Spectrometer (NMS) and the Ion Mass Spectrometer (IMS; Krankowsky et al. 1986; Balsiger et al. 1987). The use of neutral and ionospheric models was necessary to interpret the collected data set and it is still an ongoing effort (Balsiger et al. 1986; Allen et al. 1987; Geiss et al. 1991; Altwegg et al. 1993; Rubin et al. 2011). Molecular oxygen was generally not suspected around Halley. Indeed, even if the NMS and IMS measured neutrals and ions at mass 32 u, other species than O_2 and O_2^+ with similar masses could contribute to these readings, such as CH_3OH or S. However, taking into account the major sulphur-bearing species, together with CH_3OH, cannot explain the signal measured at mass 32 u/e, O_2 could be the solution (Rubin et al. 2015). The fact that O_2 was directly observed around 67P (Bieler et al. 2015), as well as O_2^+ (see Section 3.1), strengthens this argument.

Most of the previous ionospheric models assessing ion composition in a cometary coma focused on comet 1P/Halley. Haider & Bhardwaj (2005) presented a very comprehensive study. With a high outgassing rate, ion-neutral collisions unlock complex chemical pathways and the final ion composition appears very different from the neutral composition. For example, minor elements, such as nitrogen N, represented by ammonia NH_3 (among others) in the neutral population ($\approx$1 per cent volume mixing ratio), is the parent of NH_4^+ which is expected to be the main ion at low cometocentric distances during high-activity conditions (Beth et al. 2016). The crossing of a diamagnetic cavity out to about 4000–4500 km from Halley, detected during *Giotto*'s fly-by (Neubauer et al. 1986), facilitated the interpretation of ion-neutral interactions as ions are not directly picked up by the solar wind motional field but move slowly in a field-free plasma. When studying 67P/C-G ion composition, it is therefore relevant to focus on the near-perihelion period where the outgassing was sufficiently high to allow more ion-neutral collisions and thus more chemical pathways. A diamagnetic cavity was also intermittently detected near perihelion (Goetz et al. 2016a,b) with the onboard RPC/MAGnetometer (MAG; Glassmeier et al. 2007b). Even though the cavity was only detected during short time spans, it seems to be a global structure around the nucleus during high-activity periods (Henri et al. 2017). The ionospheric model presented here was first developed by Vigren & Galand (2013) and predicted the formation of NH_4^+ from the protonation reaction of ammonia NH_3. Thanks to the high-mass resolution of ROSINA/DFMS, the NH_4^+ peak could be unambiguously distinguished from the H_2O^+ peak at mass 18 u (Beth et al. 2016). The ionospheric model was updated and used to predict ion masses 19 u to 18 u ratios near perihelion in Fuselier et al. (2016). Mass 19 u (H_3O^+) dominates over mass 18 u (H_2O^+) in the inner characteristic region described by Mandt et al. (2016). In this region, though still magnetized, the average ion energies are relatively low (1–10 eV), of the order of the spacecraft potential (Odelstad et al. 2015; Eriksson et al. 2017).

This paper presents the ions detected by ROSINA/DFMS. Our interpretation of the different spectra is driven by the use of an ionospheric model. Section 2 gives an in-depth review of the model. The real-time neutral number density and neutral species volume mixing ratios are taken into account in the model in order to compute the ion composition at the location of *Rosetta*. In particular, we focus on ions resulting from the protonation of HPA neutrals. Results are discussed for two typical dates, both near perihelion. Section 3 focuses on the detection by ROSINA/DFMS of the protonated version of HPA neutrals. The origin of other ion species appearing in the analysed spectra is also discussed. Then, we evaluate instrumental properties that affect ROSINA/DFMS ion measurements. Section 4 is a summary comparison of the ions detected and interpreted around comet 67P/C-G and those detected around 1P/Halley.

2 IONOSPHERIC MODEL

The ionospheric model is an improved version of the one first proposed by Vigren & Galand (2013). The present version is driven by a fluid neutral model we recently developed (in-depth review in

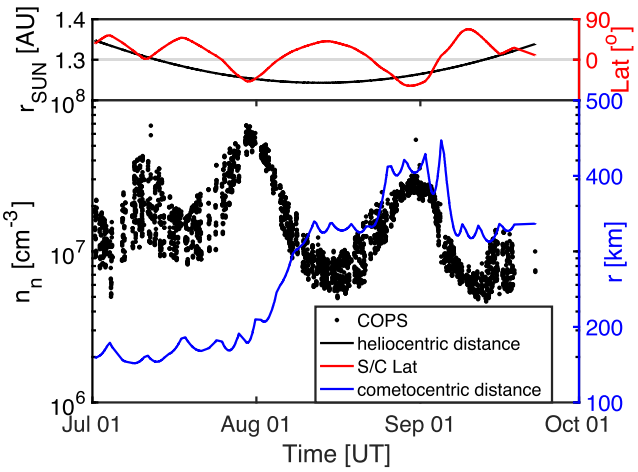

Figure 1. Top: time series of the heliocentric distance (black curve) and sub-spacecraft latitude (red curve). Bottom: time series of measured ROSINA/COPS uncorrected neutral number densities (black dots) and cometocentric distance (blue curve). The data set stops on 2015 September 22, the start of the excursion to high cometocentric distances.

Appendix A). More neutral species (besides the original H_2O and CO) and an updated chemical library, containing a more detailed ion-neutral and electron-ion dissociative recombination reactions (see Tables B1 and B2) were added. Section 2.1 describes the observed neutral environment during the near-perihelion period and explains how the neutral model integrates the information acquired by ROSINA/COPS. Section 2.2 gives a review of the ionospheric model and the different assumptions that are made. Finally, Section 2.3 presents some results of the ionospheric model.

2.1 Neutral background

A one-dimensional (1D) neutral model was developed to improve the accuracy of the ionospheric model. It relies on an adiabatic fluid expansion around the nucleus. The details are provided in Appendix A. This approach was used in order to characterize the cooling of the neutral population (and to use these temperatures for the ion-neutral kinetic coefficients) and the increase in outflow velocity as the cometary gas moves away from the nucleus. Global 3D kinetic models have been developed to describe the neutral population of 67P (Fougere et al. 2016a,b; Tenishev et al. 2016). Near perihelion, and close to the nucleus (0–1000 km), computationally cheaper fluid-like approaches give similar results to a global kinetic model along the radial direction, as shown in Fig. A1. The model needs to be calibrated with boundary conditions, which for a fluid model need to be specified at the top of the Knudsen layer (Crifo & Rodionov 1997; Crifo et al. 2002). Near perihelion, the Knudsen layer is expected to be around 5 m above the surface of the nucleus of comet 67P (Tenishev et al. 2008). As it is small compared to the mean cometocentric distance at the surface (2 km), we therefore place the Knudsen layer at the surface of the nucleus for the rest of this study.

It is possible to measure with good accuracy the neutral density at the location of the spacecraft thanks to the ROSINA/COPS. Fig. 1 shows the total neutral number density as a function of time over the time window considered. During this period, the spacecraft was near perihelion (1.24 au on 2015 August 13). The neutral density measured by ROSINA/COPS does not change significantly and oscillates around 10^7 cm^{-3} within an order of magnitude, with

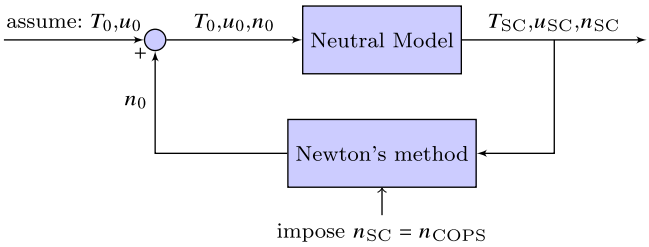

Figure 2. Schematic of the numerical scheme adopted to constrain boundary condition at the surface. Neutral surface temperature T_0 and surface neutral outflow u_0 are arbitrary fixed. A Newton method is used to find the neutral number density n_0 at the surface such that the neutral number density at the cometocentric distance of the spacecraft n_{SC} computed by the model is equal to what is actually measured by ROSINA/COPS.

small-scale variations driven by the rotation of the comet (Hässig et al. 2015; Hansen et al. 2016). However, the local neutral activity greatly changes over this period as the measured neutral density has to be put in context with the cometocentric distance and the latitude (seasonal) effects. Taking the product of the neutral observed density with the square of the cometocentric distances, we can estimate the local neutral activity. The nr^2 product reached its minimum on 2015 July 4 ($nr^2 = 6.5 \times 10^{23}$ m^{-1}) and its maximum on 2015 August 31 ($nr^2 = 4.8 \times 10^{24}$ m^{-1}) over the period considered. Changes in activity greatly affect the ion composition, as it can enhance or restrain chemistry (see Section 2.3).

The boundary conditions for the adiabatic neutral model are determined by fixing the outflow velocity u_0 and the temperature T_0 close to the surface of the nucleus. These conditions are fixed at $u_0 = 400$ m s^{-1} and $T_0 = 200$ K in the simulation runs presented in Section 2.3. This near-surface temperature is standard around perihelion and was derived by Davidsson & Gutiérrez (2005) from their thermophysical model. It is also in agreement with the Microwave Instrument for the *Rosetta* Orbiter (MIRO; Gulkis et al. 2007; Marshall et al. 2017) analysis. Huebner & Markiewicz (2000) gave, as an estimation of the near-surface outflow bulk velocity, 0.8257 multiplied by the mean gas speed of the Maxwell speed distribution (we find 400 m s^{-1} at 200 K). We can use a Newton method to find a value of n_0 that fulfils the conditions imposed by the COPS measurement: $n(r_{SC}) = n_{COPS}$ (the algorithm stops when the relative error between the two quantities is below 10^{-4}), where r_{SC} stands for the cometocentric distance of the spacecraft and n_{COPS} stands for the neutral density probed by ROSINA/COPS at a given time. With this method, the neutral model is driven by actual measurements and reproduces realistic conditions. This method is mapped out in Fig. 2. Using this calibration, the neutral outflow velocity profile reaches terminal velocities of about 800 m s^{-1} (see Fig. A1). It is in the same range as MIRO terminal velocity derivations under near-perihelion conditions (Marshall et al. 2017).

2.2 Ionospheric model description

The ion number densities are computed by solving the 1D continuity equation with spherical symmetry for each ion species i:

$$\frac{\partial n_i}{\partial t} + \frac{1}{r^2}\frac{\partial n_i r^2 u_i}{\partial r} = P_i^{h\nu} + P_i^{e-\text{impact}} + P_i^{\text{chem}} + n_i R_i^{e-}. \quad (1)$$

(i) n_i (m^{-3}) stands for the number density of ions of species i.

(ii) The second term on the left-hand side represents transport, where u_i (m s^{-1}) stands for the bulk velocity of the ions of species i. They are all assumed to be equal to the bulk velocity of neutrals

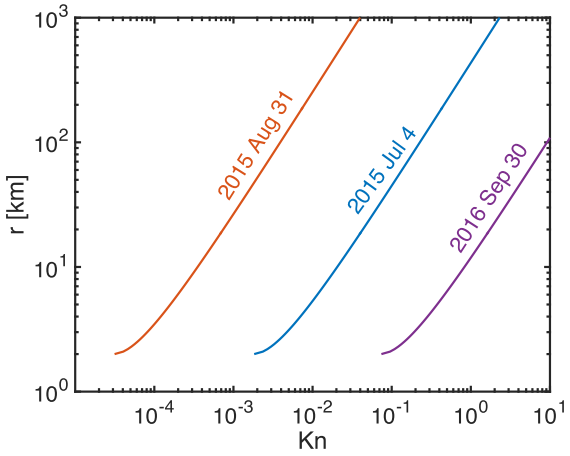

Figure 3. Computed ion-neutral Knudsen number as a function of the cometocentric distance for three different conditions. The red curve represents conditions on 2015 August 31 ($n = 3 \times 10^7$ cm^{-3} at 400 km), the blue curve represents conditions on 2015 July 4 ($n = 2 \times 10^7$ cm^{-3} at 180 km) and the purple curve represents the conditions during the end of mission on 2016 September 30 ($n = 4 \times 10^7$ cm^{-3} at 10 km).

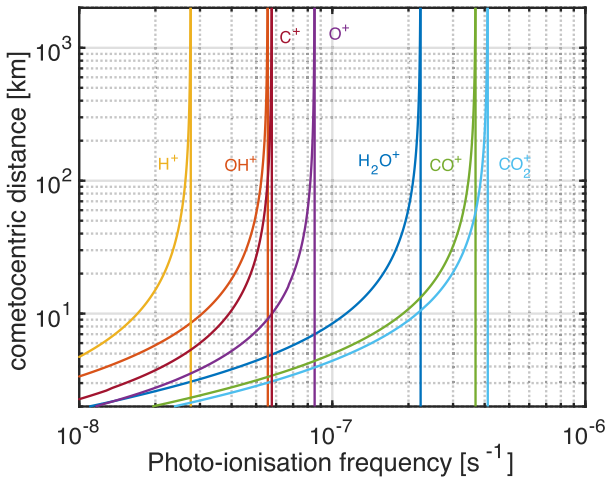

Figure 4. Computed photoionization rates for typical neutral species detected by ROSINA/DFMS in the coma of 67P. The local conditions were taken with a neutral number density of $n = 2 \times 10^6$ cm^{-3} at 400 km and a solar zenith angle of 90°. The solid lines represent the photoionization taking in account solar attenuation with Beer–Lambert law, whereas the dash–dotted lines represent the photoionization rates with no attenuation.

computed according to Section A1 (i.e. $u_i = u$ for all i) that means the ions maintain the same velocity as the neutrals. This assumption relies on the fact that the ion population collides with neutrals and has the same gas expansion profile as the neutral species. The ion population represents about a ten thousandth of the total population. The energy gained through other acceleration processes, such as the motional electric field that can take place outside the diamagnetic cavity (Goetz et al. 2016b; Mandt et al. 2016), is partially lost through inelastic collisions with neutrals. As a result, the ion outflow velocity moving away from the nucleus is the same as that for the neutral population. At sufficiently high cometocentric distances, the medium is not dense enough to maintain these collisions and the cometary ions are eventually picked up by the solar wind. Therefore, we need to verify that these collisions do happen at the cometocentric distances we are considering. Collisions are assessed by the ion-neutral Knudsen number. The Knudsen number is defined as the ratio between the mean free path and the typical scaleheight of the problem. The cometocentric distance r acts as this typical height. Note that for an r^{-2} dependence on the neutrals (equation A2), the ion scaleheight H generally defined as $H = n_i/|\nabla ni|$ is exactly r, whereas for the neutral population it is $r/2$ (Beth et al. 2016; Galand et al. 2016). The mean free path λ can be computed from the number density n and the ion-neutral cross-sectional area σ for collisions ($\lambda = (n\sigma)^{-1}$). The newly formed ions have the same energy as the kinetic energy of the parent neutral, taken to be 0.07 eV (800 m s^{-1}). The resulting H_2O^+-H_2O cross-section is $\sim 4 \times 10^{-14}$ cm^2 (Lishawa et al. 1990; Fleshman et al. 2012). Fig. 3 shows the ion-neutral Knudsen number as a function of the cometocentric distance for three different conditions. Two of them represent near-perihelion conditions with a high local neutral activity ($n\,r^2 = 4.8 \times 10^{24}$ m^{-1}) reached on 2015 August 31 (red curve) and a low local neutral activity ($n\,r^2 = 6.5 \times 10^{23}$ m^{-1}) reached on 2015 July 4 (blue curve). The third condition was taken when the comet was significantly less active, at the end of mission, in 2016 September 30 (purple curve), at 3.8 au from the Sun ($n\,r^2 = 4 \times 10^{21}$ m^{-1}, see Heritier et al. 2017). The Knudsen number is well below 1 for most of the cometocentric distances covered by *Rosetta*. However, the ion exobase is a transition region, not a strict boundary. We expect the spacecraft to be occasionally located above the ion exobase. During these times, ion acceleration can take place (Mandt et al. 2016; Vigren et al. 2017) and ions with high energies (100 eV) were detected at these periods by RPC/Ion and Electron Sensor (IES). At low cometocentric distances and below the electron exobase, a diamagnetic cavity (Goetz et al. 2016a; Henri et al. 2017) should prevent the interplanetary magnetic field to affect the ions close from the nucleus. The presence of an ambipolar electric field, preventing depart from plasma neutrality, could decouple the ion transport from that of the neutrals (Vigren & Eriksson 2017), accelerating ions up to speeds of few kilometres per second at the location of *Rosetta* and slowing down the electrons. It is however still unclear how the ambipolar electric field varies as a function of the cometocentric distances and local conditions.

(iii) $P_i^{h\nu}(r)$ (m^{-3} s^{-1}) stands for the production of ion species i through photoionization by solar Extreme UltraViolet (EUV) radiation. It is computed from the solar irradiance measured at Earth by the Thermosphere Ionosphere Mesosphere Energetics and Dynamics (TIMED)/Solar EUV Experiment (SEE; Woods et al. 2005). Observations were taken on 2015 July 15 and extrapolated to comet 67P to take into account the decrement due to higher heliocentric distance (≈1.3 au). Apart from the heliocentric distance, the solar flux is not subject to important changes over the period considered. For photoionization sourcing, we considered the three most abundant species in the coma: H_2O (the parent of H_2O^+, OH^+, H^+, O^+), CO_2 (the parent of CO_2^+, CO^+, C^+, O^+) and CO (the parent of CO^+, C^+, O^+). The photoionization cross-sections are taken from Vigren & Galand (2013) for H_2O and CO and from Cui et al. (2011) for CO_2. We compute the solar attenuation of the flux travelling through the column of atmosphere using the Beer–Lambert law (Schunk & Nagy 2009). Near perihelion, the atmosphere is thick enough in the EUV range to affect the photoionization rate. This attenuation is illustrated in Fig. 4, where the photoionization rates of different chemical species are plotted as a function of the cometocentric distance. Solid lines represent the photoionization rates using the Beer–Lambert law, and the dash–dotted lines represent the rates without taking into account solar absorption. The latter are associated with total photoionization frequencies at 1.3 au of

$3.13 \times 10^{-7}\,s^{-1}$, $5.05 \times 10^{-7}\,s^{-1}$ and $3.49 \times 10^{-7}\,s^{-1}$ for H_2O, CO_2 and CO, respectively. Local conditions were taken with a typical outgassing rate in August 2015 ($n = 2 \times 10^6\,cm^{-3}$ at 400 km). A solar zenith angle of 90° is assumed as *Rosetta*'s orbit was close to the terminator plane during most of this period. The effect of solar attenuation is significant, confirming the findings of Vigren & Galand (2013). The rates decrease by an entire order of magnitude in the last 10 km above the surface. While this attenuation of the solar EUV radiation influences the ion composition, it does not affect the total ion density at the location of the spacecraft (150–400 km near perihelion) because each cometocentric distance is contributing uniformly to the total amount. For instance, an attenuated ionization frequency in the first 10 km only affects by 5 per cent the total number density of ions present at 200 km.

(iv) $P_i^{e-\text{impact}}$ ($m^{-3}\,s^{-1}$) stands for the production of the ion species i by electron-impact ionization. This ionization frequency can be computed from RPC/IES (Burch et al. 2007) at the location of the spacecraft. The method is described in Galand et al. (2016). Here, it is found to be non-significant with a magnitude of about $3 \times 10^{-8}\,s^{-1}$ (compared to the photoionization frequency of $3.13 \times 10^{-7}\,s^{-1}$ for H_2O). The suprathermal electron flux undergoes energy degradation as it penetrates into the coma. However, an additional source of this suprathermal population can be the energetic photoelectrons typically produced by soft X-ray solar radiation in thicker parts of the coma. This is an important ionization source around comet 1P/Halley as pointed out by Cravens et al. (1987) and Haider & Bhardwaj (2005). Their contribution was evaluated in the case of 67P by Vigren & Galand (2013). It was found that the energetic photoelectrons are not abundant enough to make a significant contribution to the overall ionization rate due to the thin atmosphere of comet 67P in comparison to comet 1P, even at perihelion. Consequently, electron-impact ionization is too weak near perihelion and is neglected in every simulation presented here. This statement is not true for high heliocentric distances, as photoionization scales with its inverse square root. In October 2014, at 3.15 au from the Sun, RPC/IES measured suprathermal electron fluxes that were intense enough at times to be the dominant source of ionization (Galand et al. 2016). On 2016 September 30, at the end of mission (3.8 au), electron-impact ionization was also found to dominate over photoionization (Heritier et al. 2017).

(v) $P_i^{\text{chem}}(r, t)$ ($m^{-3}\,s^{-1}$) stands for the net production of the ion species i by ion-neutral chemical reactions (positive if production and negative for a loss of ion species i). The list of reactions with their respective kinetic coefficients are presented in Table B1. The temperature used for the kinetic coefficients is taken from the neutral model output and is a decreasing function of the cometocentric distance (see Fig. A1). We focus on the chemical pathways involving HPA neutrals. Proton affinity (PA) characterizes the ability of a neutral to capture a proton (H^+) from a protonated species. M_{HPA} is defined here as a neutral species in the coma that has a higher PA than that of H_2O such that the following reaction is efficient:

$$H_3O^+ + M_{HPA} \rightarrow H_2O + M_{HPA}H^+. \quad (2)$$

H_3O^+ is an abundant species in the ionosphere of comet 67P, especially near perihelion (Fuselier et al. 2016). Any reaction involving it with significant kinetic coefficients is therefore relevant and affects the ion composition. This phenomenon was explained in detail by Beth et al. (2016) for the specific case of NH_4^+ (protonated NH_3). In this paper, we review other ion species associated with HPA neutrals that can affect the ion composition with the same kind of reaction chains. A schematic of the main chemical pathways leading to the production and loss of protonated HPA neutrals M_{HPA} is given in Fig. 5.

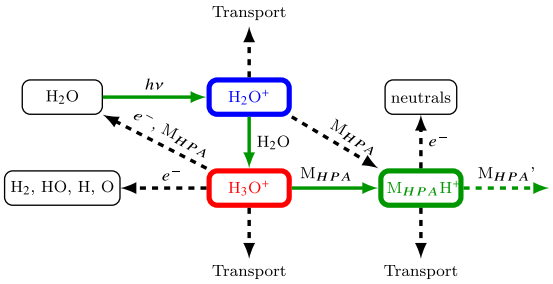

Figure 5. Chemical pathways in the ionosphere of comet 67P showing the effect of M_{HPA} neutrals. H_2O is ionized to give H_2O^+. H_2O^+ efficiently reacts with H_2O to create H_3O^+. If the coma is dense enough, H_3O^+ can then react with M_{HPA} if PA (M_{HPA}) > PA(H_2O). If this new $M_{HPA}H^+$ is not NH_4^+ (terminal), it can possibly react with a neutral M_{HPA}' having an even higher proton affinity PA (M_{HPA}') > PA (M_{HPA}). Ions can also be lost through electron-ion dissociative recombination and transport.

Table 1. List of the neutrals with higher PA than H_2O detected in the coma of 67P near perihelion and their respective PA.

M_{HPA}	PA (eV)
H_2O	7.17
H_2S	7.32
H_2CO	7.40
HCN	7.40
CH_3OH	7.83
NH_3	8.86

(vi) R_i^{e-} (s^{-1}) stands for the electron-ion dissociative recombination rate of ion species i with an electron. The list of the associated rate constants is provided in Table B2. The electron temperature is assumed to be constant at 200 K (~0.02 eV). It is a bit lower than the 0.065 eV found by Eriksson et al. (2017) at the location of *Rosetta* near perihelion. However, we must take in account the fact that the electrons undergo collisions – thus cooling – with neutrals as the electron exobase is always above the surface near perihelion (whereas it is under the surface at high heliocentric distances; Heritier et al. 2017) and occasionally very close to the spacecraft (Henri et al. 2017). Dissociative recombination affects both ion composition and total ion density at the location of the spacecraft during high-activity conditions, decreasing the total ion number density by about 50 per cent at 200 km.

The continuity equation (1) is solved for each spherical shell using a finite-forward difference method. Results are found by reaching equilibrium (within 0.001 per cent) in each shell between transport, chemical production and chemical loss. Typical time-scales of the different terms were computed and presented in Beth et al. (2016).

2.3 Model results for near-perihelion conditions

A list of the HPA neutrals detected in the coma of comet 67P by ROSINA/DFMS neutral mode during perihelion and their respective PA is displayed in Table 1. Fig. 6 depicts the neutral composition near perihelion measured by ROSINA/DFMS neutral mode from 2015 July 1 to September 15. Water vapour is by far the dominant neutral species in the coma. Carbon dioxide is usually present with

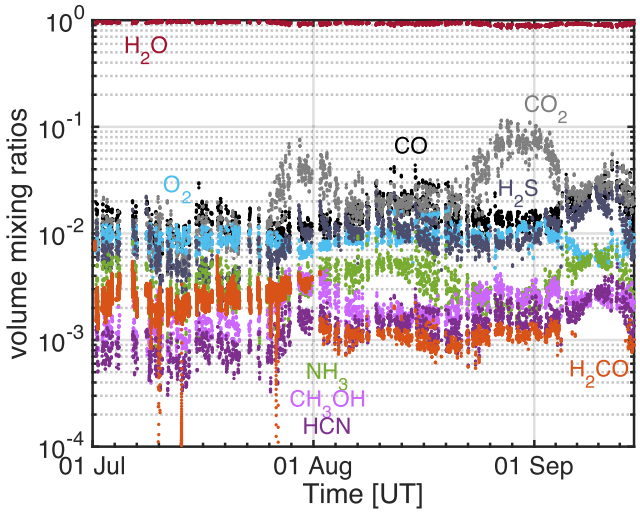

Figure 6. Time evolution of the neutral volume mixing ratios measured by ROSINA/DFMS near perihelion, from 2015 July 1 to 2015 September 15. Water, carbon dioxide, carbon monoxide, dioxygen and all the HPA neutral species referred in Table 1 are represented.

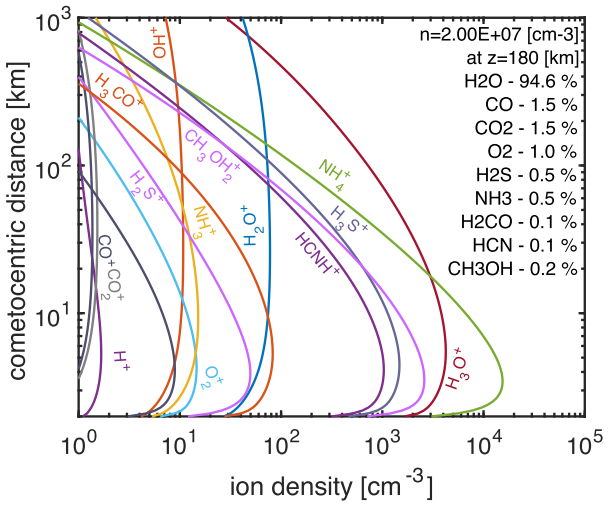

Figure 7. Modelled ion densities as a function of the cometocentric distance for neutral conditions reproducing 2015 July 4. See the top right caption for total neutral number density at the position of the spacecraft, along with neutral volume mixing ratios, which are assumed constant as a function of r.

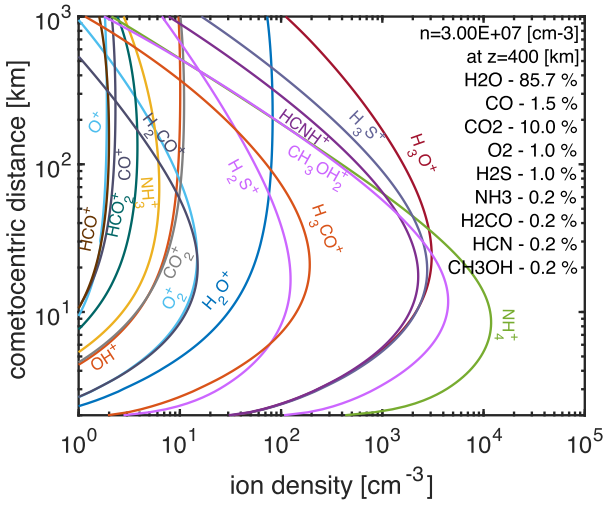

Figure 8. Same as Fig. 7 for 2015 August 31.

a volume mixing ratio up to 10 per cent at the end of August. All the other species are minor and represent 1 per cent or less of the neutral composition. H_2S and NH_3 are the most abundant HPA neutral species, as they occasionally reach 1 per cent. The other HPA neutral species, CH_3OH, HCN and H_2CO, are less abundant, and their volume mixing ratios lie between 0.1 per cent and 0.5 per cent most of the time (see Fig. 6). The neutral-ion chemical reactions associated with these chemical species are integrated into the ionospheric model (Table B1).

We ran the ionospheric model for the two extrema of the neutral activity and their different respective neutral composition. The minimum during the period studied was reached on 2015 July 4 and the maximum on 2015 August 31. The model is calibrated according to the neutral number density measured by ROSINA/COPS on these specific days: 2×10^7 cm^{-3} at 180 km for July 4 (12:20 PM) and 3×10^7 cm^{-3} at 400 km for August 31 (03:40 AM). Neutral mixing ratios are set to be constant with cometocentric distance and tuned to what was measured *in situ* by ROSINA/DFMS at the relevant time. Their values are displayed in Figs 7 and 8.

Fig. 7 shows the results of the ionospheric model for 2015 July 4 conditions. At low cometocentric distances, NH_4^+ dominates the ion composition. This is due to the high neutral densities close to the surface that promote more collisions, thus more chemical reactions. NH_3 is the detected HPA neutral with the highest PA (see Table 1). It happens to be also the HPA neutral with the highest volume mixing ratio on that date, along with H_2S. However, H_3S^+ only comes fourth in terms of ion volume mixing ratio, even at low cometocentric distances, because its PA is the lowest after water (see Table 1). Its number density is even lower than $CH_3OH_2^+$, even though CH_3OH has a volume mixing ratio (0.2 per cent) lower than H_2S (0.5 per cent). As the cometocentric distance increases, the neutral densities decrease and H_3O^+ becomes the dominant ion. This is due to the fact that the chemical pathway leading to H_3O^+ is shorter than the one for ions from a protonated HPA neutrals: it requires less collisions and involves the major neutral species H_2O, as depicted in Fig. 5. H_3O^+ (one collision needed after ionization) is easier to replenish than NH_4^+ (which requires at least two collisions). The slope of the curves above the peaks are actually similar for all the HPA neutral species as the cometocentric distance increases and the formation of new protonated ions becomes less likely: it is associated with loss by transport. Near 1000 km, when chemistry becomes too rarefied to produce H_3O^+, H_2O^+ is predicted to be the dominant ion as it is directly produced through photoionization. At sufficiently low cometocentric distances (<1000 km here), H_2O^+ remains in the state of photochemical equilibrium: its number density remains constant, as its depletion due to ion-neutral reactions is balanced by its production through ionization of H_2O, as long as it is not the major ion (Vigren & Galand 2013). As the cometocentric distance increases, predictions of the H_3O^+ to H_2O^+ ratios are sensitive to acceleration phenomena that are not captured by this model. A detailed study of this ratio over the perihelion period was conducted by Fuselier et al. (2016).

Conditions on 2015 August 31 were drastically different from that of on July 4. The neutral densities were significantly higher ($\sim$ a factor of 4) than in July (when normalized to the same cometocentric distance). This greatly affects the ion-neutral chemistry, solar attenuation (see Section 2.2) and thus the overall shapes of the

ionospheric density profiles. Neutral composition was also significantly different as H_2S was the most abundant HPA neutral (see Fig. 6). However, at low cometocentric distances, NH_4^+ is still dominating even if NH_3 is less abundant (see Fig. 8). This is not only due to the difference in kinetic coefficients between the reactions $H_3O^+ + NH_3 \rightarrow H_2O + NH_4^+$ and $H_3O^+ + H_2S \rightarrow H_2O + H_3S^+$. In fact, PA is not directly linked to the magnitude of these kinetic coefficients (see Tables 1 and B1). This is due to the fact that there are more chemical pathways leading to NH_4^+; protons can travel between several HPA neutral species as long as the new one has a higher PA. For example, H_2S can steal a proton from H_3O^+ that can then be stolen by NH_3. Every path leads to NH_4^+, as NH_3 has the highest PA. However, some paths are longer than others. As the cometocentric distance increases, reactions involving three or more reactions are less likely to happen. That is why H_3S^+ ion density takes over NH_4^+ at about 40 km. The carbon dioxide volume mixing ratios greatly changed between the two days considered; however, the impact of CO and CO_2 on the ion-neutral chemistry is insignificant as our model has shown (Fuselier et al. 2016). The main outcome is only the creation of $HCO^+$and HCO_2^+.

The results from these simulations can be put in context with the ROSINA/DFMS ion mode measurements presented in Section 3. Our ionospheric model is able to predict which species are expected to be detected, to derive the ion density ratios and to help interpret the measurements.

3 ROSINA/DFMS OBSERVATIONS

3.1 Detection of protonated version of HPA neutrals

The ROSINA/DFMS instrument can detect ionospheric species in the coma when it operates in ion mode. A high-resolution (HR) mode allows the instrument to distinguish ion species with very similar masses [$m/\Delta m > 3000$ at 1 per cent peak height on the 28 u/e mass per charge (Balsiger et al. 2007)]. The low resolution (LR) has a reduced mass resolution, with $m/\Delta m$ of about several hundred, but has a higher sensitivity which is crucial to detect rarefied species.

Ions entering the sensor are accelerated to a potential $V_{\rm accel}$ such that their mass/charge ratio is suitable to make it through the analyser section [$V_{\rm accel}$ proportional to $(m/q)^{-1}$]. The ions are first deflected by 90° in an electrostatic analyser and then by 60° in a permanent magnet before hitting the micro channel plate (MCP) detector. The suitable acceleration potential depends on the mass/charge; therefore, each mass/charge has to be measured sequentially, separated by approximately 30 s. The offset of the MCP/Linear Electron Detector Array (LEDA) is removed via a fit through a third-order polynomial. The gain of each pixel consists of the overall gain, which depends on the detector voltage, and the individual pixel gain. The pixel gain changed throughout the mission, as the central pixels received a higher lifetime change. The individual pixel gain was monitored regularly over the mission by moving the same ion beam across detector and comparing the obtained signal. Afterwards, the number of ions can be derived from the corresponding counts on the detector (Le Roy et al. 2015). Finally, a mass scale can be derived according to the calibration function presented in Beth et al. (2016). For each pixel, a statistical error is proportional to the square root of the number of counts and is shown in the spectra of Fig. 9. There are also systematic errors on the gains used that should be less than 10 per cent.

Among all the HPA species listed in Table 1, we have detected a protonated version of every single one of them with ROSINA/DFMS over the perihelion period. Examples of the corresponding spectra

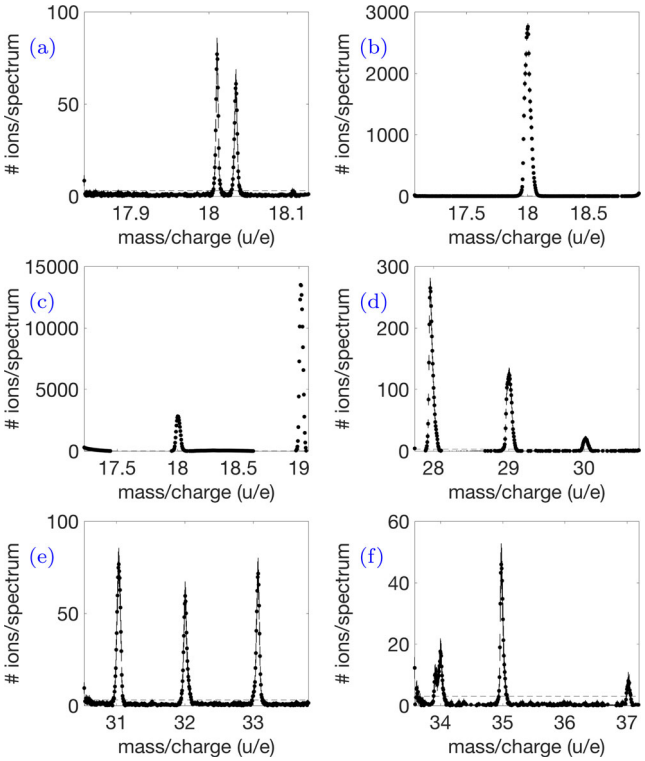

Figure 9. ROSINA-DFMS spectra showing detection of protonated HPA neutrals. We can see signatures of H_2O^+ (18.015 u/e) and NH_4^+ (18.038 u/e) in HR in panel (a); NH_4^+ (18 u/e, overlapping with H_2O^+) in panel (b); H_3O^+ (19 u/e) in LR in panel (c); $HCNH^+$ (28 u/e, overlapping with CO^+ in LR), HCO^+ (29 u/e) and H_2CO^+ (30 u/e) in panel (d); H_3CO^+ (31 u/e), CH_3OH^+ (32 u/e, together with S^+ and O_2^+) and $CH_3OH_2^+$ (33 u/e) in panel (e); H_2S^+ (34 u/e), H_3S^+ (35 u/e) in panel (f).

Table 2. List of the different mass peaks observed in Fig. 9 and their corresponding ions.

Mass/charge	Associated species	Alternatives
18 u/e	H_2O^+, NH_4^+	–
19 u/e	H_3O^+	–
28 u/e	$HCNH^+$, CO^+	–
29 u/e	HCO^+	–
30 u/e	H_2CO^+	NO^+
31 u/e	H_3CO^+	HNO^+
32 u/e	CH_3OH^+, S^+, O_2^+	–
33 u/e	$CH_3OH_2^+$	SH^+
34 u/e	H_2S^+, $^{34}S^+$	–
35 u/e	H_3S^+	–
37 u/e	$H_3{}^{34}S^+$, C_3H^+, H_2O-H_3O^+	–

are provided in Fig. 9. Table 2 provides the main corresponding ions for the different mass peaks.

Fig. 9(a) shows a HR spectrum centred around 18 u/e. Near this mass, the two most abundant ions are H_2O^+ (18.015 u/e) and NH_4^+ (18.038 u/e). The HR of the instrument permitted the first direct detection of NH_4^+ in cometary comae (Beth et al. 2016). Fig. 9(b) shows an LR spectrum centred around the same mass. The two species cannot be disentangled at this mass resolution. As NH_3 is the HPA species with the highest PA, NH_4^+ was regularly detected in the coma near perihelion.

Fig. 9(c) represents an LR scan of mass/charge 18 and 19 u/e. The peak at mass/charge 19 u/e corresponds to H_3O^+: its count number

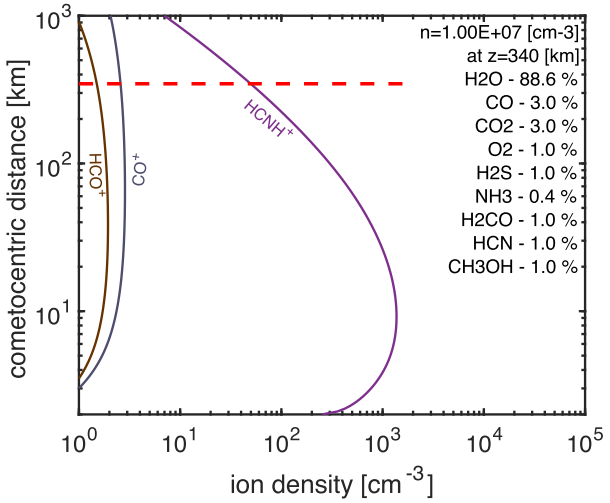

Figure 10. Computed ion density profiles of $HCNH^+$, CO^+ and HCO^+. The model is calibrated for the neutral gas environment on 2015 August 22. At the position of *Rosetta*, indicated by the dashed red line (340 km), the model predicts $HCNH^+$ to be more abundant than CO^+.

is significantly higher than the ones for all the other ions present in Fig. 9 and higher than the peak at 18 u/e next to it. As seen in the simulations of Section 2.3, H_3O^+ is predicted to be dominant at the position of *Rosetta*. There are, however, some LR spectra at different dates, where mass 18 dominates (Beth et al. 2016; Fuselier et al. 2016).

Fig. 1 (d) shows an LR spectrum of masses per charge 28, 29 and 30 u/e. The peak at mass/charge 28 u/e could be $HCNH^+$ (28.018 u/e) or CO^+ (27.994 u/e). The HR mode used to distinguish H_2O^+ from NH_4^+ at mass/charge 18 u/e is sometimes compromised at other masses as the decrease in sensitivity brings the two mass peaks below the background level. The ionospheric model is here required to identify the main ion species that contributed to the peaks. This spectrum was taken on 2015 August 22. By calibrating the model to the local conditions (COPS total neutral number density and DFMS neutral composition on 2015 August 22, see legend in Fig. 10), we have computed the number density profiles of these two ions in order to estimate their density profiles, as shown in Fig. 10. *Rosetta* was at a cometocentric distance of 340 km. $HCNH^+$ is predicted to be present and even to dominate over CO^+. $HCNH^+$ is therefore making a significant contribution to the 28 u/e peak. The model proves to be useful not only to compute and predict ion densities but also to interpret *in situ* data. The presence of CO^+ predicted by the model is also consistent with the presence of a peak at 29 u/e. The peak at mass/charge 29 u/e is certainly associated with HCO^+ resulting from the chemistry of CO^+ with H_2O (see Table B1). Actually, CO^+ and HCO^+ are very correlated as Rubin et al. (2009) pointed it out in the case of comet 1P/Halley. For lower activity conditions, at higher heliocentric distances, Fuselier et al. (2015) discussed the HCO^+ to CO^+ ratios in the case of 67P. Whenever CO is present, it is likely to get ionized and react with H_2O, whereas H_2O^+, which is constantly present, is likely to react with neutral CO to produce HCO^+. When looking at a large number of spectra over the mission, we can see that one is generally detected with the other. The peak at mass/charge 29 u/e could also be associated with $C_2H_5^+$ from a chemical reaction between C_2H_4 and HCO^+. However, Luspay-Kuti et al. (2015) explained that the detection of C_2H_4, in the neutral mode of ROSINA/DFMS, is likely due to the fragmentation of heavier hydrocarbons in the instrument. For the same reason, we do not associate $C_2H_4^+$ (from the possible ionization of C_2H_4 or charge-exchange between C_2H_4 and H_2O^+) to the peak at mass/charge 28 u/e. The fact that the peak at 29 u/e (only associated with HCO^+) is significantly lower than the peak at 28 u/e on the spectra confirms that $HCNH^+$ is a major contributor to 28 u/e, as predicted by the model. The peak at mass/charge 30 u/e is associated with H_2CO^+ coming from the ionization of H_2CO or charge-exchange between H_2CO and H_2O^+ (Table B1).

Fig. 9(e) shows a spectrum of mass/charge 31, 32 and 33 u/e. The peaks at mass/charge 31 and 33 u/e correspond to two protonated HPA neutrals: H_3CO^+ and $CH_3OH_2^+$, respectively. The peak at mass/charge 32 u/e could be associated with S^+ (31.97 u/e), CH_3OH^+ (32.03 u/e) or O_2^+ (31.99 u/e). On certain dates, all these ions were abundant enough to be detected in HR mode (despite the reduction in sensitivity). By looking at the differences in u/e between several mass peaks, we can disentangle these species. Most of the time we can see S^+ and CH_3OH^+. O_2^+ is also present but less often. Despite the significant volume mixing ratio of molecular oxygen in the coma (about 1 per cent, see Fig. 6), O_2^+ is very efficient at capturing electrons from other neutral species (Table B1). It is an important loss process that must be taken into consideration and reduces significantly its density.

Finally, Fig. 9(f) shows a spectrum identifying H_3S^+ on mass/charge 35 u/e, the protonated version of H_2S. On mass/charge 34 u/e, there are two peaks. The high peak is associated with H_2S^+ (33.99 u/e), resulting from photoionization of H_2S or charge-exchange between H_2O^+ and H_2S (Table B1). The second peak could be associated with $^{34}S^+$ (33.96 u/e). The origin of S is not clear yet as photodissociation of H_2S, and other sulphur-bearing species cannot explain the amount of S that is measured (Calmonte et al. 2016). Nevertheless, the main sulphur-bearing species H_2S presents an isotopic ratio $^{34}S/^{32}S \sim 0.04$ (Calmonte 2015) that could explain the peak at 34 observed by DFMS ion mode. It remains puzzling to clearly see these peaks in LR mode, so this interpretation remains open to discussion. One argument that goes in favour of the interpretation of $^{34}S^+$ is that in the same spectra, there is a peak at 37 (quite unusual) that could also be associated with $H_3{}^{34}S^+$. Around Halley, Marconi et al. (1989) identified the main contribution to the 37 u/e peak to be C_3H^+ ions, originating from CHON dust grains. A quantitative analysis would be out of the scope of this paper, but it could be a plausible candidate. Another origin or contribution to this peak could be the water ion cluster H_2O–H_3O^+. Their contribution in the Vigren & Galand (2013) ionospheric model was found to be minor at cometocentric distances higher than 100 km. However, ion water clusters were actually observed by the *Cassini* spacecraft in the Enceladus plume (Hill et al. 2012). For Halley, Marconi et al. (1989) argued that the thermodynamical conditions were unlikely to favour the formation of H_2O–H_3O^+ clusters (without excluding this possibility completely).

3.2 Statistical analysis

Measuring the number density of each ion species is not trivial. The total number of ions can be derived based on the RPC/Mutual Impedance Probe (MIP; Trotignon et al. 2007) and LAP (Eriksson et al. 2007), but the number density of each ion species cannot be measured directly. By taking the ratios between the different integrated ion counts of each ion species, one can estimate the number density ratio between two ion species, as it was done for masses/charge 19 u/e (H_3O^+) and 18 u/e (H_2O^+ or NH_4^+) by Fuselier

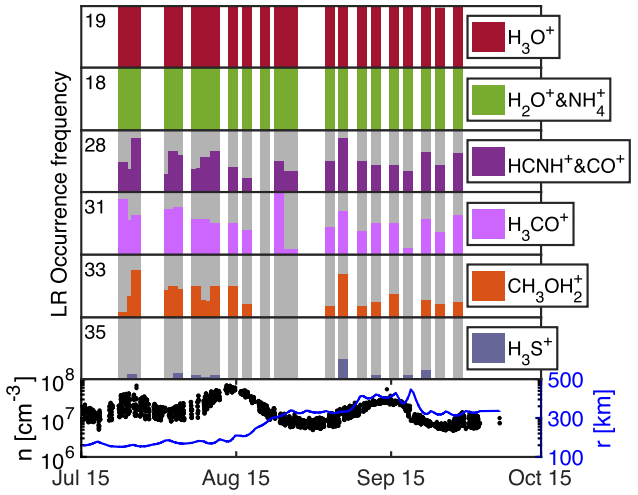

Figure 11. Time series of the occurrence frequencies (number of times an ion is spotted per day divided by the number of scans of its corresponding mass) of H_3O^+, H_2O^+ and NH_4^+ in LR together, $HCNH^+$ and CO^+ in LR together, H_3O^+, $CH_3OH_2^+$ and H_3S^+ during the 2015 July-to-September period. The bottom panel corresponds to the associated COPS number density (black dots) and the cometocentric distance (blue line) for context.

et al. (2015) and Fuselier et al. (2016). Some problems are still persistent with this approach:

(i) The spectra are not taken simultaneously (Balsiger et al. 2007). For example, there is about 30 s between LR scans for one mass to the next. Therefore, integrated ion count ratios cannot be taken at the exact same time and external conditions may have varied in between.

(ii) In LR modes, some masses can be attributed to two or more ions.

(iii) The narrow field of view of DFMS and the interaction with the solar wind through electric and magnetic fields can drive ions out of the field of view of ROSINA/DFMS (Fuselier et al. 2015). We are, therefore, only sampling a small part of the full-ion distribution.

(iv) The spacecraft potential can accelerate the ions enough to push them out of the energy acceptance window and this effect is mass dependent (see Section 3.3).

Due to these effects, we have chosen to apply a statistical approach to the detection of ions by ROSINA/DFMS. We base our analysis on the simple binary information determining whether there is a detection of a specific ion or not. A detection here is defined as a spectral speak above the background level (i.e. spectral peak above the background level, for which we take an upper-bound of three ion counts per spectrum, similar to Beth et al. 2016). For each day, we introduce the occurrence frequency – or relative frequency – f_i for an ion of mass/charge i defined as below:

$$f_i = \frac{\text{Number of times the ion species of mass/charge i is detected}}{\text{Number of DFMS ion scans of mass/charge i}}. \quad (3)$$

Fig. 11 shows the time series over the near-perihelion period of $f_{18}, f_{19}, f_{28}, f_{31}, f_{33}$ and f_{35} in LR mode, respectively, corresponding to the following ions: H_2O^+ or NH_4^+, H_3O^+, $HCNH^+$ or CO^+, H_3CO^+, $CH_3OH_2^+$ and H_3S^+. The occurrence frequencies of H_3O^+ and (H_2O^+, NH_4^+) stagnate at 1 during the whole period. This is consistent with the model results and the production mechanisms explained in Section 2.2. H_3O^+ results from a reaction between H_2O^+ and H_2O. As water dominates the composition, it is expected to happen. As it is a one-collision reaction chain, this ion is also detected during low-activity periods (Fuselier et al. 2015). H_2O^+ is produced directly by ionization of water. It is detected during low-activity periods (Fuselier et al. 2015) and dominates ion composition when ions undergo significant acceleration (Fuselier et al. 2016). Reaction chains yielding the protonation of NH_3 can produce NH_4^+ that contributes to f_{18}. It is frequently detected in HR mode over the near-perihelion period considered here (Beth et al. 2016).

The other ion species $HCNH^+$, H_3CO^+, $CH_3OH_2^+$ and H_3S^+ are detected less often. Just like NH_4^+, their production mechanisms are the protonation of HPA neutrals (see Fig. 5 and Table 1). Even if their occurrence frequencies are less than 1, they are detected most of the time during the near-perihelion period. Ion-neutral reactions involving two or more collisions happen near the nucleus. The bottom panel of Fig. 11 shows the time evolution of the total neutral density obtained with ROSINA/COPS and the cometocentric distance of *Rosetta*. It can be seen that the detection of these ions is correlated with high COPS neutral densities combined with small cometocentric distances or very high outgassing rates. Detections are frequent in July 2015 due to small cometocentric distances and, frequent in the second half of August 2015 and the first half of September due to high activity (high number densities despite the large cometocentric distances). The ion density profiles are extremely sensitive to neutral conditions, as shown in Figs 7 and 8. By examining Fig. 11 closely, one can notice the following trend: the heavier an ion species, the less frequent its detection. This could be explained by the effects of the spacecraft potential on the energy acceptance and the mass sensitivity of the instrument, as discussed in the next section.

3.3 Energy acceptance and sensitivity of the instrument

When ions enter the instrument, they are accelerated with a potential V_{accel} proportional to $(m/q)^{-1}$ (Schläppi 2011). The energy acceptance of the DFMS electrostatic analyser is 1 per cent. DFMS is set to a nominal ion energy of 20 eV. Therefore, only ions with an energy within the range of 20 eV $\pm$ 0.01$|V_{\text{accel}}|$e are accepted. For example, for mass/charge 18 u/e the acceleration voltage is $\sim$3441 V; therefore, H_2O^+ ions need to have an energy between -14.4 eV (measuring effectively 0 eV) and 54.4 eV to pass through the electrostatic analyser. This energy window covers low- and high-energy ions. However, for heavy ions, such as H_3S^+ at mass/charge 35 u/e, the acceleration voltage is only $\sim$1764 V. Therefore, H_3S^+ ions need to be in the energy range of 2.36–37.64 eV to make it through the analyser section. The heavier the ion, the smaller the energy acceptance window.

When ions are created from their neutral parents, they have an energy of about 0.1 eV. The photon energy – minus the ionization threshold energy – goes to the photoelectron, so the energy newly born ions have is very close to the kinetic energy of the parent neutral (around 1 km s^{-1}). Moreover, the ambient motional electric field can start accelerating them as soon as they are formed, and water group ions with an energy up to 100 eV have occasionally been detected by RPC/IES (Burch et al. 2007) and RPC/Ion Composition Analyzer (Nilsson et al. 2007). These energetic ions were usually detected when *Rosetta* was located beyond the boundary described by Mandt et al. (2016), where collisions with neutral species are too rare to be able to slow down these ions and the acceleration processes freely take place. It is therefore possible for ions to end up outside the energy acceptance window, especially for heavy ions.

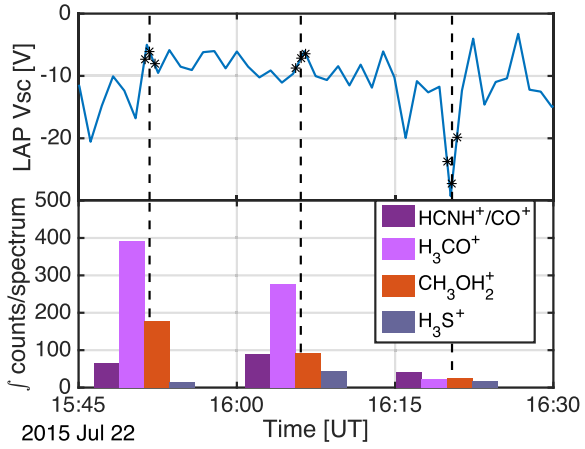

Figure 12. Top: time series of the spacecraft potential probed by RPC/LAP on 2015 July 22 from 15:45 to 16:30 UT, the black stars correspond to the times at which the DFMS spectra were taken, by a group of three, always in the following order: 28 u/e, then 31 and 33 u/e together, and finally 35 u/e. Bottom: integrated peak ion counts of the DFMS spectra for $HCNH^+/CO^+$ (28 u/e), H_3CO^+ (31 u/e), $CH_3OH_2^+$ (33 u/e) and H_3S^+ (35 u/e). The vertical black dashed lines correspond to the average time at which each group of DFMS spectra was taken.

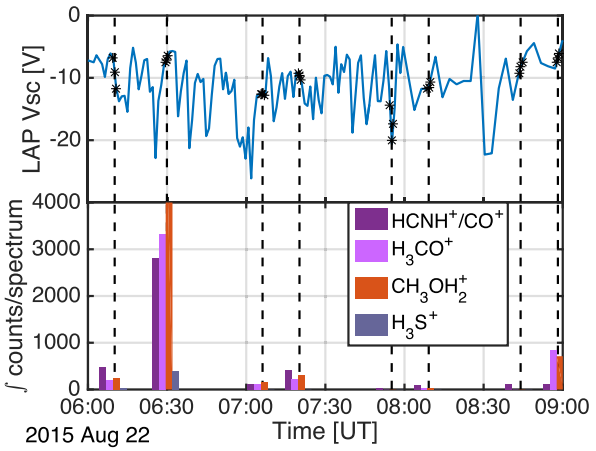

Figure 13. Same as Fig. 12, except for 2015 August 22 from 06:00 to 09:00 UT.

This discrimination related to mass is amplified in the case of highly negative spacecraft potentials. RPC/LAP (Eriksson et al. 2007) recorded negative spacecraft potentials between 0 and −30 V during the entire near-perihelion period. Ions are thus accelerated just before reaching the DFMS instrument. For the extreme case of −30 V, an H_3S^+ ion would therefore need to have an initial energy below 7.64 eV for detection. This is a heavily discriminating criterion, especially when *Rosetta* is located beyond the ion exobase.

The RPC/LAP and ROSINA/DFMS data set were used to assess this effect. Fig. 12 shows the time evolution of the RPC/LAP spacecraft potential (LAP V_{sc}, the top panel) on 2015 July 22 from 15:45 to 16:30 UT. The potentials were corrected with an α factor (Odelstad et al. 2015) of 1.2 to take into account the inhomogeneity of the plasma along the LAP1 boom (LAP1 is the only boom used here). It is quite a small correction, as the plasma is dense near perihelion with an ion density of the order of 1100 cm^{-3} (Eriksson et al. 2017), so the length of the LAP1 boom (2.24 m) is larger than the Debye length (of the order of 1 m). We compare this potential to the ROSINA/DFMS spectra that were taken during the same period. The bottom panel shows the integrated ion counts per spectrum for $HCNH^+$ and CO^+ (28 u/e), H_3CO^+ (31 u/e), $CH_3OH_2^+$ (33 u/e) and H_3S^+ (35 u/e). The black stars over the top panel LAP V_{sc} potential indicate the exact time at which the three spectra were taken. They are always taken in the following order: 28 u/e, then 31–33 u/e together (share the same spectrogram, as shown in Fig. 9 e) and finally, 35 u/e. Additionally, the vertical black line joining the two panels indicates the average time at which each group of three spectra was taken.

The effect of the spacecraft potential on the ion counts at masses 28–35 u/e is noticeable. The integrated counts of ions are higher for higher (less negative) spacecraft potentials. The variability in the spacecraft potential is important, it can go from −5 to −30 V in less than 5 min. The neutral conditions do not have enough time to vary significantly during such a short time span though the detected ion population is clearly changing. The correlation between V_{sc} and high-mass ion counts seems to be real and can be attributed to the energy acceptance of the instrument. It affects heavy ions more strongly than lighter ions.

Fig. 13 shows the same analysis performed exactly a month after, on 2015 August 22. Neutral conditions were different compared with 2015 July 22 (Fig. 12) as the spacecraft was farther away from the nucleus but the neutral density was similar (Fig. 1) due to higher outgassing rates. The effect of the spacecraft potential is also present: there is very low or zero ion detection for very negative spacecraft potentials, whereas the highest integrated counts of ions occur for the scans with the highest (least negative) associated spacecraft potential. There are many other examples that illustrate this effect. The ion composition depends on many other parameters but the fact that we can see this correlation seems to indicate that the spacecraft potential actively perturbs the energy range of DFMS ion mode and thereby the detection of heavy ions.

Another effect is the decrease in sensitivity due to the terminal velocity of ions in the DFMS instruments (Schläppi 2011). The terminal velocity v of the ions in DFMS is proportional to the square root of the energy over the mass ($v = \sqrt{2E/m}$). The final energy E itself is strongly dependent on the acceleration voltage V_{accel} in addition to the spacecraft potential and the initial ion energy. As stated before, V_{accel} is proportional to $(m/q)^{-1}$. There is therefore a decreasing sensitivity with increasing mass.

Both sensitivity and energy acceptance are dependent on mass. These two discriminating effects are adding together. Many parameters are involved in the final ion composition but the ion counts tend to be lower for heavy ions than light ions for similar number densities. This could explain the decrease in occurrence frequency with increasing masses shown in Fig. 11 and the fact that H_3S^+ is rarely detected despite the presence of H_2S (with a volume mixing ratio of 1–2 per cent) and the induced importance of its protonated version found in the ionospheric model (see Section 2.3).

4 ION DETECTION: 67P/C-G VERSUS 1P/HALLEY

The *Giotto* spacecraft encountered Comet Halley on 1986 March 13. Aboard, the IMS was composed of two major subsystems. The High Energy Range Spectrometer (HERS) was designed to measure energetic ions outside the contact surface, whereas the High Intensity Spectrometer (HIS) measured ions inside the contact surface. Both sensors are discussed in detail by Balsiger et al. (1987). The ions reported at comet 67P in this paper (Section 3) were all detected

Table 3. List of the ions mentioned in this paper with the protonated species presented in Table 1 colourized. Each species (directly detected or inferred from the use of ionospheric models to interpret the observed mass peaks) around 67P/C-G and 1P/Halley is referred in the respective columns.

ion	Mass/charge (u/e)	C-G 67P/*Rosetta*	Halley 1P/*Giotto*
H_2O^+	18	Fuselier et al. (2015)	Balsiger et al. (1986); Altwegg et al. (1993)
NH_4^+	18	Beth et al. (2016)	Allen et al. (1987); Altwegg et al. (1993)
H_3O^+	19	Fuselier et al. (2015)	Balsiger et al. (1986); Altwegg et al. (1993)
CO^+	28	”	”
$HCNH^+$	28	This paper	Geiss et al. (1991)
HCO^+	29	Fuselier et al. (2015)	”
H_2CO^+	30	This paper	”
H_3CO^+	31	”	”
S^+	32	”	”
O_2^+	32	”	Eberhardt et al. (1994)
CH_3OH^+	32	”	Geiss et al. (1991)
$CH_3OH_2^+$	33	”	”
H_2S^+	34	”	Marconi et al. (1990); Geiss et al. (1991)
H_3S^+	35	”	Marconi et al. (1990); Geiss et al. (1991)
C_3H^+ (possible)	37	”	Marconi et al. (1989)

around Halley by the IMS. Some mass peaks were interpreted with no ambiguity, such as mass/charge 31 u/e (H_3CO^+), while others, such as 18 u/e (H_2O^+, NH_4^+), needed the use of ionospheric models or further studies to interpret them. In this section, we discuss how the IMS spectra were interpreted for mass peaks that could hide two or more ions. We summarize the list of ions reported in Section 3.1, which were also detected by *Giotto*, in Table 3 with the associated references.

Water group ions including H_2O^+ and H_3O^+ were first identified by Balsiger et al. (1986), the 16–19 u/e range was then discussed in detail by Altwegg et al. (1993). The mass resolution permitted the identification of ions separated by about 1 u/e in the water range. It therefore could not distinguish NH_4^+ from H_2O^+ directly from the spectra. However, Allen et al. (1987) determined that the 19 u/e to 18 u/e ratios observed could not be explained by a purely water coma but by a coma containing also NH_3, proving indirectly the detection of NH_4^+ and explaining its formation process by protonation of ammonia.

Geiss et al. (1991) conducted an extended study of the ions belonging to the 25–35 u/e mass/charge range with IMS-HIS and reported detection of CO^+, $HCNH^+$, HCO^+, H_2CO^+, H_3CO^+, S^+, CH_3OH^+, $CH_3OH_2^+$, H_2S^+ and H_3S^+, among others. The last two ions were also reported by Marconi et al. (1990). Just like around 67P (see Section 3.1), the peak at 28 is most likely associated with both CO^+ and $HCNH^+$ around 1P. CO was indeed the second most dominant molecule around Halley (Eberhardt et al. 1987). Besides, detection of HCO^+ at mass/charge 29 u/e shows that CO^+ (as well as CO) was present around Halley (Rubin et al. 2009), as it is created through chemical reaction with H_2O (or charge-exchange between CO and H_2O^+). However, Geiss et al. (1991) stated that CO^+ is expected to react efficiently by charge exchange with water (Table B1). According to their interpretation, $HCNH^+$ is expected to be the main contribution of the peak at mass/charge 28 u/e (69 per cent at 1500–2000 km from the nucleus). This conclusion is compatible with the detections of other protonated HPA neutral species around Halley, such as H_3CO^+ and $CH_3OH_2^+$. The peaks at mass/charge 31 and 33 u/e are entirely associated with these two ions, respectively. The peaks at mass/charge 32 u/e were interpreted by Geiss et al. (1991) as 62 per cent CH_3OH^+ and 38 per cent S^+ at a cometocentric distance of 1700 km from the nucleus of Halley. Their ionospheric model did not include O_2^+, ion produced from the ionization of molecular O_2. Eberhardt et al. (1994) included it in their model and estimated that it could contribute by about 4 per cent at 3500 km. These papers were written before the unexpected detection of molecular oxygen by ROSINA/DFMS (Bieler et al. 2015). A study from Rubin et al. (2015) suggested that molecular oxygen could be present around Halley with a relative abundance of about 3.8 per cent with respect to water.

The peak at mass/charge 37 u/e spotted around Halley was associated with dust-born C_3H^+ by Marconi et al. (1989). It is a plausible explanation for comet 67P as well as other candidates, such as $H_3{}^{34}S^+$ and H_2O-H_3O^+ ion clusters, for the reasons mentioned in Section 3.1.

5 CONCLUSIONS

We report for the first time the detection of ion species from the protonation of HPA neutrals and other processes in the mass/charge range of 28–37 u/e. The ionospheric model for the coma of comet 67P was significantly improved with respect to its previous versions (Vigren & Galand 2013; Fuselier et al. 2015; Beth et al. 2016; Fuselier et al. 2016). The use of an adiabatic neutral expansion in the background of our ionospheric model gives us some constraints on the neutral outflow bulk velocity, neutral temperature used for the ion-neutral kinetic coefficients and the neutral number density. It also shows that for near-perihelion conditions, a computationally cheap fluid model gives similar results as a global kinetic Direct Simulation Monte Carlo (DSMC) model (Section A2) but is limited along the comet-spacecraft line. The fact that it is easy to run makes it possible to calibrate the near-surface boundary condition to ROSINA/COPS neutral densities at the location of the spacecraft (Section 2.1) and at any given time.

The main source of ions near perihelion is photoionization, whereas the contribution of electron-impact ionization is significantly less at that time than in other periods of the mission, such as in September 2016 (Heritier et al. 2017). Absorption of solar EUV radiation by the coma is crucial to compute accurate photoionization rates close to perihelion for the near-nucleus region (Fig. 4).

The ion-neutral chemical data base (Table B1) was updated to take into account all the HPA neutrals and other major neutral species in the coma. It seems that CO and CO_2 have little to no contribution to the ion-neutral chemistry, as it was shown in

Fuselier et al. (2016). Other minor neutral species that have an HPA, such as NH_3, H_2CO, HCN and CH_3OH, are not abundant in the coma (<1 per cent volume mixing ratio) but can, however, have a significant impact on the ion population. Their ability to steal a proton from H_3O^+ (which is often the main ion species) make them very competitive with respect to other neutrals in terms of ion-neutral chemistry. This efficiency is increased close from the nucleus, where collisions are more likely. We predict that protonated HPA neutrals are dominating the ion composition at low cometocentric distances near perihelion (Figs 7 and 8). In terms of elements, the neutral composition does not reflect the ion composition (NH_4^+ dominates over H_2O^+ and H_3O^+ even if H_2O is vastly more present than NH_3) at low cometocentric distances. At higher distances, the medium rarefies and chemical pathways resulting in protonated neutrals need too many collisions to occur and maintain high mixing ratios. Therefore, ions with simpler chemistry (H_3O^+) or no chemistry at all (H_2O^+, CO_2^+) gain in relative importance (see Section 2.3).

These model predictions were assessed by ROSINA/DFMS ion mode data analysis. In the near-perihelion period, the spacecraft was located relatively far from the nucleus (150–400 km, see Fig. 1). All the protonated versions of the HPA neutrals (H_3S^+, H_3CO^+, $HCNH^+$, $CH_3OH_2^+$ and NH_4^+) were detected by ROSINA/DFMS (Section 3.1), only NH_4^+ was previously reported in the coma of 67P (Beth et al. 2016). They are not abundant, but it is expected by the model at these cometocentric distances. We identified additional ions reported for the first time around 67P, such as HCO^+, H_2CO^+, S^+, $CH_3OH_2^+$ and O_2^+. We also suspect the presence of some peculiar ions, such as $^{34}S^+$, $H_2{}^{34}S^+$ or C_3H^+. Other isotopic ions in the water family are suspected to appear in our spectra but are out of the scope of this paper and are left to further studies. The relative detection frequency of these ions seems to be negatively correlated with the ion mass (Section 3.2). Some instrumental effects are likely to explain this. Ions can be driven out of the energy acceptance window when the spacecraft is negatively charged. It would affect primarily heavy ions as the acceleration voltage within the instrument is inversely proportional to the mass (Schläppi 2011), thus the upstream acceleration related to the spacecraft potential gains in relative importance (Section 3.3). This is clearly illustrated by lower ion count readings at very negative spacecraft potentials when cross comparing ROSINA/DFMS and RPC/LAP data set (Fig. 13). Another discriminating criteria to heavy ions could come from the sensitivity dependent on the final velocity of the ions. These effects, as well as the calibration of the ion spectra, need to be carefully taken care of before evaluating the ion mixing ratios solely from a data analysis perspective.

The ions reported in Section 3 were also detected by *Giotto* around comet 1P/Halley. In some cases, their interpretation relies primarily on ionospheric model results and some assumptions made on the coma neutral composition. Some additional work could also be done in interpreting the ionosphere of Halley now that we have further constraints on the neutral composition of comet 67P. The *Rosetta* mission gave us clues not only to decrypt the environment of comet 67P, but also to improve our current understanding of the environment of other comets as well. It is interesting to ask the question: what are the new pieces of information that the *Rosetta* mission brought for the study of Halley? The detection of NH_4^+ by ROSINA/DFMS HR (Beth et al. 2016) and NH_3 by ROSINA/DFMS neutral mode confirmed the interpretation of Allen et al. (1987). Molecular O_2 was unexpected, but it was detected around 67P (Bieler et al. 2015) together with O_2^+ in this study. O_2 is now suspected around Halley (Rubin et al. 2015). Finally, the detection of H_3S^+, H_3CO^+, $HCNH^+$ and $CH_3OH_2^+$ around comet 67P is consistent with the interpretation made by Geiss et al. (1991) in the 28–35 u mass range spectra harvested around Halley.

ACKNOWLEDGEMENTS

Work at Imperial College London is supported by Imperial College President's scholarship and STFC of UK under grants ST/K001051/1 and ST/N000692/1. Work on ROSINA at the University of Bern was funded by the State of Bern, the Swiss National Science Foundation and the ESA PRODEX Program. Work at BIRA-IASB was supported by the Belgian Science Policy Office via PRODEX/ROSINA PEA90020 and 4000107705 and by the FRS-FNRS grant PDR T.1073.14 'Comparative study of atmospheric erosion'. We are indebted to the ROSINA operation and data processing teams. We acknowledge the MIRO team for providing us with information ahead of publication. We acknowledge the staff of CDDP and Imperial College London for the use of AMDA and the RPC Quicklook data base (provided by a collaboration between the Centre de Données de la Physique des Plasmas, supported by CNRS, CNES, Observatoire de Paris and Université Paul Sabatier, Toulouse and Imperial College London, supported by the UK Science and Technology Facilities Council). Work at Swedish Institute of Space Physics is supported by the Swedish National Space Board (166/14). Work at Southwest Research Institute is supported with contract through the Jet Propulsion Laboratory.

REFERENCES

Adams N., Smith D., Grief D., 1978, Int. J. Mass Spectrom. Ion Phys., 26, 405
Adams N. G., Smith D., Paulson J. F., 1980, J. Chem. Phys., 72, 288
Allen M., Delitsky M., Huntress W., Yung Y., Ip W.-H., 1987, A&A, 187, 502
Altwegg K. et al., 1993, A&A, 279, 260
Anicich V. G., 1993, J. Phys. Chem. Ref. Data, 22, 1469
Balsiger H. et al., 1986, Nature, 321, 330
Balsiger H. et al., 1987, J. Phys. E: Sci. Instrum., 20, 759
Balsiger H. et al., 2007, Space Sci. Rev., 128, 745
Benna M., Mahaffy P. R., 2006, Geophys. Res. Lett., 33, L10103
Beth A. et al., 2016, MNRAS, 462, S562
Bieler A. et al., 2015, Nature, 526, 678
Brian J., Mitchell A., 1990, Phys. Rep., 186, 215
Burch J. L., Goldstein R., Cravens T. E., Gibson W. C., Lundin R. N., Pollock C. J., Winningham J. D., Young D. T., 2007, Space Sci. Rev., 128, 697
Calmonte U. M., 2015, PhD thesis, Physikalisches Institut der Universität Bern
Calmonte U. et al., 2016, MNRAS, 462, S253
Copp N., Hamdan M., Jones J., Birkinshaw K., Twiddy N., 1982, Chem. Phys. Lett., 88, 508
Cravens T. E., 1997, Physics of Solar System Plasmas. Cambridge University Press, Cambridge
Cravens T. E., Kozyra J. U., Nagy A. F., Gombosi T. I., Kurtz M., 1987, J. Geophys. Res. (Space Phys.), 92, 7341
Crifo J. F., Rodionov A. V., 1997, Icarus, 129, 72
Crifo J. F., Lukianov G. A., Rodionov A. V., Khanlarov G. O., Zakharov V. V., 2002, Icarus, 156, 249
Cui J., Galand M., Coates A. J., Zhang T. L., Müller-Wodarg I. C. F., 2011, J. Geophys. Res. (Space Phys.), 116, A04321
Davidsson B. J. R., Gutiérrez P. J., 2005, Icarus, 176, 453
Eberhardt P. et al., 1987, A&A, 187, 481
Eberhardt P., Meier R., Krankowsky D., Hodges R. R., 1994, A&A, 288, 315
Eriksson A. I. et al., 2007, Space Sci. Rev., 128, 729

Eriksson A. I. et al., 2017, A&A, in press
Filippi A., Occhiucci G., Speranza M., 1997, Inorg. Chem., 36, 3936
Flammer K. R., Mendis D. A., 1993, J. Geophys. Res., 98, 21
Fleshman B. L., Delamere P. A., Bagenal F., Cassidy T., 2012, J. Geophys. Res. (Planets), 117, E05007
Fougere N. et al., 2016a, MNRAS, 462, S156
Fougere N. et al., 2016b, A&A, 588, A134
Freeman C., Harland P., McEwan M., 1978, Int. J. Mass Spectrom. Ion Phys., 28, 19
Fuselier S. A. et al., 2015, A&A, 583, A2
Fuselier S. A. et al., 2016, MNRAS, 462, S67
Galand M. et al., 2016, MNRAS, 462, S331
Geiss J. et al., 1991, A&A, 247, 226
Geppert W. D. et al., 2006, Faraday Discuss., 133, 177
Glassmeier K.-H., Boehnhardt H., Koschny D., Kührt E., Richter I., 2007a, Space Sci. Rev., 128, 1
Glassmeier K.-H. et al., 2007b, Space Sci. Rev., 128, 649
Goetz C. et al., 2016a, MNRAS, 462, S459
Goetz C. et al., 2016b, A&A, 588, A24
Gulkis S. et al., 2007, Space Sci. Rev., 128, 561
Haider S., Bhardwaj A., 2005, Icarus, 177, 196
Hamberg M. et al., 2007, Mol. Phys., 105, 899
Hanner M. et al., 1985, Icarus, 64, 11
Hansen K. C. et al., 2007, Space Sci. Rev., 128, 133
Hansen K. C. et al., 2016, MNRAS, 462, S491
Hässig M. et al., 2015, Science, 347, aaa0276
Henri P. et al., 2017, MNRAS, 469, S372
Herbst E., Leung C. M., 1986, ApJ, 310, 378
Heritier K. et al., 2017, MNRAS, 469, S118
Hill T. W. et al., 2012, J. Geophys. Res. (Space Phys.), 117, A05209
Huebner W. F., Markiewicz W. J., 2000, Icarus, 148, 594
Huntress W. T., Jr, 1977, ApJS, 33, 495
Huntress W. T., Pinizzotto R. F., Jr, 1973, J. Chem. Phys., 59, 4742
Huntress W. T., Jr, Anicich V. G., McEwan M. J., Karpas Z., 1980, ApJS, 44, 481
Jones J., Birkinshaw K., Twiddy N., 1981, Chem. Phys. Lett., 77, 484
Kamińska M. et al., 2008, ApJ, 681, 1717
Karpas Z., Huntress W., 1978, Chem. Phys. Lett., 59, 87
Karpas Z., Anicich V., Huntress W., 1978, Chem. Phys. Lett., 59, 84
Krankowsky D. et al., 1986, Nature, 321, 326
Lamy P. L., Toth I., Davidsson B. J. R., Groussin O., Gutiérrez P., Jorda L., Kaasalainen M., Lowry S. C., 2007, Space Sci. Rev., 128, 23
Le Roy L. et al., 2015, A&A, 583, A1
Lishawa C. R., Dressler R. A., Gardner J. A., Salter R. H., Murad E., 1990, J. Chem. Phys., 93, 3196
Luspay-Kuti A. et al., 2015, A&A, 583, A4
Mandt K. E. et al., 2016, MNRAS, 462, S9
Marconi M. L., 2007, Icarus, 190, 155
Marconi M. L., Korth A., Mendis D. A., Lin R. P., Mitchell D. L., Reme H., D'Uston C., 1989, ApJ, 343, L77
Marconi M. L., Mendis D. A., Korth A., Lin R. P., Mitchell D. L., Reme H., 1990, ApJ, 352, L17
Marshall D. et al., 2017, A&A, 603, A87
McElroy D., Walsh C., Markwick A. J., Cordiner M. A., Smith K., Millar T. J., 2013, A&A, 550, A36
McEwan M. J., Anicich V. G., 2007, Mass Spectrom. Rev., 26, 281
McEwan M., Anicich V., Huntress W., 1981, Int. J. Mass Spectrom. Ion Phys., 37, 273
Mezei J. Z. et al., 2015, Plasma Sources Sci. Technol., 24, 035005
Neubauer F. M. et al., 1986, Nature, 321, 352
Nilsson H. et al., 2007, Space Sci. Rev., 128, 671
Novotný O. et al., 2010, J. Phys. Chem. A, 114, 4870
Odelstad E. et al., 2015, Geophys. Res. Lett., 42, 126
Öjekull J. et al., 2004, J. Chem. Phys., 120, 7391
Prasad S. S., Huntress W. T. Jr, 1980, ApJS, 43, 1
Rakshit A. B., Warneck P., 1980, J. Chem. Soc., Faraday Trans. 2, 76, 1084
Reinhard R., 1986, Nature, 321, 313
Rosen S. et al., 2000, Faraday Discuss., 115, 295
Rubin M., Hansen K. C., Gombosi T. I., Combi M. R., Altwegg K., Balsiger H., 2009, Icarus, 199, 505
Rubin M., Tenishev V. M., Combi M. R., Hansen K. C., Gombosi T. I., Altwegg K., Balsiger H., 2011, Icarus, 213, 655
Rubin M., Altwegg K., van Dishoeck E. F., Schwehm G., 2015, ApJ, 815, L11
Schläppi B., 2011, PhD thesis, Physikalisches Institut der Universität Bern
Schunk R., Nagy A., 2009, Ionospheres – Physics, Plasma Physics, and Chemistry. Cambridge University Press, Cambridge
Semaniak J. et al., 2001, ApJS, 135, 275
Smith D., Adams N. G., 1981, MNRAS, 197, 377
Smith D., Adams N. G., Henchman M. J., 1980, J. Chem. Phys., 72, 4951
Smith D., Spanel P., Mayhew C. A., 1992, Int. J. Mass Spectrom. Ion Process., 117, 457
Tanaka K., Mackay G. I., Bohme D. K., 1978, Can. J. Chem., 56, 193
Tanner S. D., Mackay G. I., Bohme D. K., 1979, Can. J. Chem., 57, 2350
Tenishev V., Combi M., Davidsson B., 2008, ApJ, 685, 659
Tenishev V. et al., 2016, MNRAS, 462, S370
Trotignon J. G. et al., 2007, Space Sci. Rev., 128, 713
Vigren E., Eriksson A. I., 2017, AJ, 153, 150
Vigren E., Galand M., 2013, ApJ, 772, 33
Vigren E. et al., 2017, MNRAS, 469, S142
Woods T. N. et al., 2005, J. Geophys. Res. (Space Phys.), 110, A01312

APPENDIX A: NEUTRAL MODEL

A1 Adiabatic model

We consider a 1D, spherical comet for which the neutral gas is radially propagating from the nucleus. The full approach is detailed by (Cravens 1997, chapter 6). The outflow bulk velocity $\boldsymbol{u(r)}$ can be written as

$$\boldsymbol{u(r)} = u(r)\hat{r}. \tag{A1}$$

We assume no local production in the coma (i.e. the gas is only coming from the sublimation of volatiles in the nucleus) and steady-state conditions. The continuity equation applied to the total neutral gas number density can be rewritten as

$$n(r)u(r)r^2 = n(r_0)u(r_0)r_0^2, \tag{A2}$$

where $n(r)$ is the neutral number density at a cometocentric distance r and r_0 stands for the radius of the nucleus (assumed to be 2 km here). We assume an ideal gas under an isentropic expansion. Gravity and neutral-dust friction are neglected. Combining momentum and energy equations yields

$$\left(M(r)^2 - 1\right)\frac{\mathrm{d}M}{M(r)} - \left(\frac{\gamma - 1}{2}M(r)^2 + 1\right)\frac{2\mathrm{d}r}{r} = 0, \tag{A3}$$

where M stands for the Mach number and γ stands for the heat capacity ratio. For molecule with six degrees of freedom, such as H_2O, $\gamma = 4/3$. There is no explicit solution for M as a function of r; however, we can express r as a function of M:

$$\frac{r}{r_0} = \sqrt{\frac{M_0}{M(r)}}\left(\frac{1 + \frac{\gamma-1}{2}M(r)^2}{1 + \frac{\gamma-1}{2}M_0^2}\right)^{\frac{\gamma+1}{4(\gamma-1)}}. \tag{A4}$$

When the boundary conditions at the surface are known, M can be computed numerically as a function of r, either from (A4) using Newton's method, or by integrating (A3) with a finite difference method. From M, one can derive the speed of sound C_s from momentum and Bernouilli equations:

$$C_s^2(r) = \frac{\frac{\gamma}{\gamma-1}\widetilde{R}T_0 + \frac{1}{2}u_0^2}{\frac{1}{\gamma-1} + \frac{1}{2}M(r)^2}, \tag{A5}$$

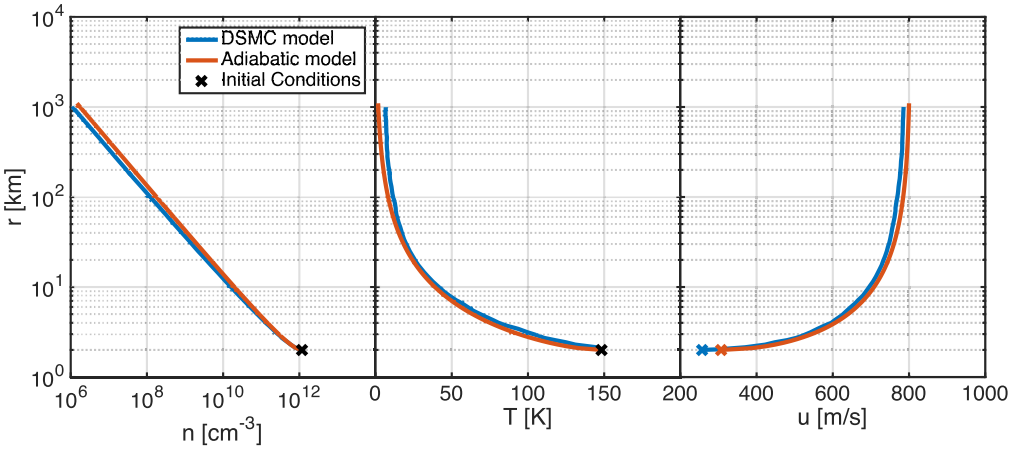

Figure A1. Comparison of the adiabatic model presented in Section A1 and a kinetic DSMC model used in Tenishev et al. (2008, for the subsolar case) in terms of neutral number density n, the temperature of the neutrals T (here H_2O), neutral bulk velocity u near perihelion conditions around comet 67P. The blue curve corresponds to the output of the full kinetic model, whereas the red curve corresponds to the output of the isentropic model. Surface conditions for neutral number density and neutral temperature are identical, but initial conditions for the outflow velocity are slightly different.

where $\widetilde{R}$ stands for the specific gas constant, and T_0 and u_0 are the temperature and bulk velocity of the outflowing gas at the surface, respectively.

From the speed of sound, one can derive the outflow velocity as a function of r. The neutral gas density can then be retrieved from equation (A2). Temperature and pressure can be calculated from the usual isentropic relations. The full system can be solved but requires boundary conditions at the surface of the nucleus.

A2 Comparison with a DSMC kinetic approach

The neutral model presented in Section A1 is a fluid model. It relies on continuum mechanics. It is sometime not appropriate to adopt this approach in a rarefied medium, such as the coma of comet 67P. Indeed, under non-equilibrium conditions, macroscopic variables, such as the temperature and the pressure, are not properly defined. A fluid approach is not valid and one must adopt a kinetic approach to describe the full physics. We confront our model to a global kinetic model in order to measure its validity. In Tenishev et al. (2008), a global kinetic model based on the DSMC method is applied to the coma of 67P. We have compared the subsolar outputs from the DSMC model used in Tenishev et al. (2008) to those from our current hydrodynamic model. Fig. A1 shows the results of this comparison on three physical parameters: the neutral number density n, the neutral temperature T and the outflow bulk velocity u. These three parameters are the ones that are used as input in the ionospheric model of Section A1. Boundary conditions for the adiabatic model are taken to be similar to those from the DSMC simulations. For the neutral number density n and the temperature T, boundary conditions at the surface (2 km from the centre) are identical and equal to 1.14×10^{12} cm^{-3} and 148 K, respectively. It corresponds to a near-perihelion high-activity situation with a heliocentric distance of 1.3 au. We expect the hydrodynamic approach to match the kinetic one for high-activity conditions, such as this one.

For the neutral outflow velocity, the boundary condition had to be taken slightly different. The kinetic model assumed 257 m s^{-1} at the surface. Such a speed yields a subsonic flow at the surface and using the Mach equation (A3) from this surface condition would not describe the physics correctly, as an expanding subsonic gas slows down. The observed coma and full kinetic models agree on the fact that the gas is accelerating and cooling. The surface outflow velocity boundary condition in our model is therefore boosted up to 307 m s^{-1}, leaving a Mach number just slightly supersonic ($M = 1.02$).

We find excellent agreement between our adiabatic model and the full kinetic model for the neutral number density and the neutral temperature as a function of the cometocentric distance r. The pressure curves are not shown here but invoking the ideal gas law yields the same agreement between the two approaches. There is a good agreement between the trends of the two outflow velocity profiles besides the shift in the near surface values that were induced by different boundary conditions. The neutral number density has a magnitude proportional to r^{-2} as predicted by the Haser model for practically all cometocentric distances. It is only near the surface that this power-law ceases to be respected. Both kinetic and isentropic models predict a larger decrement.

For near-perihelion conditions, it is therefore possible to compute these macro parameters with an hydrodynamic approach, even for a small comet like 67P. The near-perihelion neutral Knudsen numbers given by Tenishev et al. (2008) lie between 0.1 and 0.3 for the cometocentric distances considered. It is a bit higher than the 0.1 limit given by Marconi (2007) to state that the conditions are fully collisional but this transition region seems to be suitable to use a fluid model in order to compute the averaged macroscopic parameters in Fig. A1. The fluid model is computationally cheaper than a global kinetic model. Therefore, the temperature, pressure, number density and outflow velocity can be computed instantly and integrated as inputs in the ionospheric model (see Section 2), while being calibrated with respect to ROSINA/COPS neutral density measurements at the location of the spacecraft (see Section 2.1).

APPENDIX B: KINETIC RATE COEFFICIENTS

Table B1 provides the ion-neutral reaction kinetic coefficients used in the ionospheric model presented in Section 2. The list of reactions is not exhaustive and focuses on the reactions associated with a high kinetic rates or involving neutral species with a high volume mixing ratio in the coma of comet 67P. Most of these kinetic rates were measured at 300 K (McElroy et al. 2013). However, dipole locking

Table B1. List of the ion-neutral chemical reaction kinetic rates used in the ionospheric model presented in Section 2. This list is not exhaustive and focuses on reactions with high kinetic coefficients and/or involving a highly concentrated neutral species.

Reaction	Kinetic coefficient ($cm^3\ s^{-1}$)	Temperature range (K)	Reference
$H^+ + H_2O \rightarrow H_2O^+ + H$	$6.90 \times 10^{-9}\ (300/T)^{1/2}$	10–41 000	Smith, Spanel & Mayhew (1992)
$OH^+ + H_2O \rightarrow H_2O^+ + OH$	$1.59 \times 10^{-9}\ (300/T)^{1/2}$	10–41 000	Huntress & Pinizzotto (1973)
$OH^+ + H_2O \rightarrow H_3O^+ + O$	$1.30 \times 10^{-9}\ (300/T)^{1/2}$	10–41 000	Huntress & Pinizzotto (1973)
$OH^+ + HCN \rightarrow HCNH^+ + O$	$1.20 \times 10^{-9}\ (300/T)^{1/2}$	10–41 000	Prasad & Huntress (1980)
$OH^+ + CO \rightarrow HCO^+ + O$	8.40×10^{-10}	10–41 000	Anicich (1993)
$OH^+ + H_2CO \rightarrow H_3CO^+ + O$	$1.12 \times 10^{-9}\ (300/T)^{1/2}$	10–41 000	Karpas & Huntress (1978)
$OH^+ + H_2CO \rightarrow H_2CO^+ + OH$	$7.44 \times 10^{-10}\ (300/T)^{1/2}$	10–41 000	Karpas & Huntress (1978)
$OH^+ + H_2S \rightarrow H_2S^+ + OH$	$1.23 \times 10^{-9}\ (300/T)^{1/2}$	10–41 000	Jones, Birkinshaw & Twiddy (1981)
$OH^+ + CO_2 \rightarrow HCO_2^+ + O$	1.44×10^{-9}	10–41 000	Jones et al. (1981)
$H_2O^+ + H_2O \rightarrow H_3O^+ + OH$	$2.10 \times 10^{-9}\ (300/T)^{1/2}$	10–41 000	Huntress & Pinizzotto (1973)
$H_2O^+ + CO \rightarrow HCO^+ + OH$	5.0×10^{-10}	10–41 000	Jones et al. (1981)
$H_2O^+ + H_2S \rightarrow H_3S^+ + OH$	$6.8 \times 10^{-10}\ (300/T)^{1/2}$	10–41 000	Jones et al. (1981)
$H_2O^+ + H_2S \rightarrow H_2S^+ + H_2O$	$8.4 \times 10^{-10}\ (300/T)^{1/2}$	10–41 000	Jones et al. (1981)
$H_2O^+ + NH_3 \rightarrow NH_4^+ + OH$	$9.45 \times 10^{-10}\ (300/T)^{1/2}$	10–41 000	Anicich (1993)
$H_2O^+ + NH_3 \rightarrow NH_3^+ + OH$	$2.21 \times 10^{-9}\ (300/T)^{1/2}$	10–41 000	Anicich (1993)
$H_2O^+ + H_2CO \rightarrow H_3CO^+ + OH$	$7.74 \times 10^{-10}\ (300/T)^{1/2}$	10–41 000	Karpas & Huntress (1978)
$H_2O^+ + H_2CO \rightarrow H_2CO^+ + H_2O$	$1.41 \times 10^{-9}\ (300/T)^{1/2}$	10–41 000	Anicich (1993)
$H_2O^+ + HCN \rightarrow HCNH^+ + OH$	$2.10 \times 10^{-9}\ (300/T)^{1/2}$	10–41 000	McEwan et al. (1981)
$H_2O^+ + HCN \rightarrow H_3O^+ + CN$	$1.05 \times 10^{-9}\ (300/T)^{1/2}$	10–41 000	McEwan & Anicich (2007)
$H_2O^+ + O_2 \rightarrow O_2^+ + H_2O$	4.60×10^{-10}	10–41 000	Rakshit & Warneck (1980)
$H_3O^+ + NH_3 \rightarrow NH_4^+ + H_2O$	$2.20 \times 10^{-9}\ (300/T)^{1/2}$	10–41 000	Smith, Adams & Henchman (1980)
$H_3O^+ + HCN \rightarrow HCNH^+ + H_2O$	$3.80 \times 10^{-10}\ (300/T)^{1/2}$	10–41 000	Anicich (1993)
$H_3O^+ + H_2CO \rightarrow H_3CO^+ + H_2O$	$3.40 \times 10^{-9}\ (300/T)^{1/2}$	10–41 000	Tanner, Mackay & Bohme (1979)
$H_3O^+ + CH_3OH \rightarrow CH_3OH_2^+ + H_2O$	$2.50 \times 10^{-9}\ (300/T)^{1/2}$	10–41 000	Anicich (1993)
$H_3O^+ + H_2S \rightarrow H_3S^+ + H_2O$	$1.90 \times 10^{-9}\ (300/T)^{1/2}$	10–41 000	Tanaka, Mackay & Bohme (1978)
$CO^+ + H_2O \rightarrow CO + H_2O^+$	$1.79 \times 10^{-9}\ (300/T)^{1/2}$	10–41 000	Huntress et al. (1980)
$CO^+ + H_2O \rightarrow HCO^+ + CO$	$8.84 \times 10^{-10}\ (300/T)^{1/2}$	10–41 000	Huntress et al. (1980)
$CO^+ + H_2CO \rightarrow H_2CO^+ + CO$	$1.35 \times 10^{-9}\ (300/T)^{1/2}$	10–41 000	Adams, Smith & Grief (1978)
$CO^+ + H_2CO \rightarrow HCO^+ + HCO$	$1.65 \times 10^{-9}\ (300/T)^{1/2}$	10–41 000	Anicich (1993)
$CO^+ + H_2S \rightarrow H_2S^+ + CO$	$2.44 \times 10^{-9}\ (300/T)^{1/2}$	10–41 000	Anicich et al., Unpublished results
$CO^+ + NH_3 \rightarrow NH_3^+ + CO$	$2.02 \times 10^{-9}\ (300/T)^{1/2}$	10–41 000	Huntress et al. (1980)
$CO^+ + CO_2 \rightarrow CO_2^+ + CO$	1.00×10^{-9}	10–41 000	Adams et al. (1978)
$HCNH^+ + H_2CO \rightarrow H_3CO^+ + HCN$	$1.05 \times 10^{-9}\ (300/T)^{1/2}$	10–41 000	Freeman, Harland & McEwan (1978)
$HCNH^+ + NH_3 \rightarrow NH_4^+ + HCN$	$1.10 \times 10^{-9}\ (300/T)^{1/2}$	10–41 000	Huntress (1977)
$O_2^+ + NH_3 \rightarrow NH_3^+ + O_2$	$2.00 \times 10^{-9}\ (300/T)^{1/2}$	10–41 000	Adams, Smith & Paulson (1980)
$O_2^+ + H_2CO \rightarrow H_2CO^+ + O_2$	$2.07 \times 10^{-9}\ (300/T)^{1/2}$	10–41 000	Adams et al. (1980)
$O_2^+ + H_2S \rightarrow H_2S^+ + O_2$	$1.40 \times 10^{-9}\ (300/T)^{1/2}$	10–41 000	Adams et al. (1980)
$H_2CO^+ + H_2O \rightarrow H_3O^+ + HCO$	$2.60 \times 10^{-9}\ (300/T)^{1/2}$	10–41 000	Adams et al. (1978)
$H_2CO^+ + H_2CO \rightarrow H_3CO^+ + HCO$	$3.20 \times 10^{-9}\ (300/T)^{1/2}$	10–41 000	Adams et al. (1978)
$H_2CO^+ + NH_3 \rightarrow NH_4^+ + HCO$	$1.28 \times 10^{-9}\ (300/T)^{1/2}$	10–41 000	Adams et al. (1978)
$H_2CO^+ + NH_3 \rightarrow NH_3^+ + H2CO$	$7.40 \times 10^{-10}\ (300/T)^{1/2}$	10–41 000	Anicich (1993)
$H_2CO^+ + HCN \rightarrow HCNH^+ + HCO$	$1.40 \times 10^{-9}\ (300/T^{1/2}$	10–41 000	Huntress (1977)
$H_2CO^+ + CH_3OH \rightarrow CH_3OH_2^+ + HCO$	$2.16 \times 10^{-9}\ (300/T)^{1/2}$	10–41 000	Adams et al. (1978)
$H_3CO^+ + H_2O \rightarrow H_3O^+ + H_2CO$	$2.30 \times 10^{-10}\ (300/T)^{1/2}$	10–41 000	Karpas, Anicich & Huntress (1978)
$H_3CO^+ + NH_3 \rightarrow NH_4^+ + H_2CO$	$2.30 \times 10^{-9}\ (300/T)^{1/2}$	10–41 000	Huntress (1977)
$H_3CO^+ + CH_3OH \rightarrow CH_3OH_2^+ + H_2CO$	$1.90 \times 10^{-9}\ (300/T)^{1/2}$	10–41 000	Filippi, Occhiucci & Speranza (1997)
$H_3CO^+ + HCN \rightarrow HCNH^+ + H_2CO$	$1.30 \times 10^{-9}\ (300/T)^{1/2}$	10–41 000	Freeman et al. (1978)
$CH_3OH_2^+ + NH_3 \rightarrow NH_4^+ + CH_3OH$	$1.00 \times 10^{-9}\ (300/T)^{1/2}$	10–41 000	
$H_2S^+ + H_2O \rightarrow H_3O^+ + HS$	$8.10 \times 10^{-10}\ (300/T)^{1/2}$	10–41 000	Smith & Adams (1981)
$H_2S^+ + NH_3 \rightarrow NH_4^+ + HS$	$1.36 \times 10^{-9}\ (300/T)^{1/2}$	10–41 000	Smith & Adams (1981)
$H_2S^+ + H_2S \rightarrow H_3S^+ + HS$	$1.00 \times 10^{-9}\ (300/T)^{1/2}$	10–41 000	Smith & Adams (1981)
$H_3S^+ + HCN \rightarrow HCNH^+ + H_2S$	$1.50 \times 10^{-9}\ (300/T)^{1/2}$	10–41 000	Tanaka et al. (1978)
$H_3S^+ + H_2CO \rightarrow H_3CO^+ + H_2S$	$2.20 \times 10^{-9}\ (300/T)^{1/2}$	10–41 000	Tanner et al. (1979)
$H_3S^+ + NH_3 \rightarrow NH_4^+ + H_2S$	$1.90\times 10^{-9}\ (300/T)^{1/2}$	10–41 000	Smith & Adams (1981)
$CO_2^+ + H_2O \rightarrow H_2O^+ + CO_2$	$2.04 \times 10^{-9}\ (300/T)^{1/2}$	10–41 000	Karpas et al. (1978)
$CO_2^+ + NH_3 \rightarrow NH_3^+ + CO_2$	$1.90 \times 10^{-9}\ (300/T)^{1/2}$	10–41 000	Copp et al. (1982)
$CO_2^+ + H_2S \rightarrow H_2S^+ + CO_2$	$1.40 \times 10^{-9}\ (300/T)^{1/2}$	10–41 000	Copp et al. (1982)

effects increase these coefficients at low temperatures (Herbst & Leung 1986), following a modified Arrhenius law proportional to $T^{-1/2}$. In this study, we applied this temperature dependence to ion-neutral reactions involving molecules with a strong dipole moment: NH_3 (1.24 D), CH_3OH (1.69 D), H_2O (1.85 D), H_2CO (2.3 D) and HCN (2.98 D). However, we ignored the temperature dependence for ion-neutral reactions involving neutral molecules with a low-dipole moment: CO (0.1 D), CO_2 (0 D) and O_2 (0 D). Table B2

Table B2. List of the electron-ion dissociative recombination kinetic rates of the mains ion species involved in the ionospheric model presented in Section 2.

Reaction	kinetic coefficient ($cm^3\ s^{-1}$)	Temperature range (K)	Reference
$H_2O^+ + e^- \rightarrow O + H_2$	$3.90 \times 10^{-8}\ (300/T_e)^{1/2}$	10–41 000	Rosen et al. (2000)
$H_2O^+ + e^- \rightarrow O + H + H$	$3.05 \times 10^{-7}\ (300/T_e)^{1/2}$	10–1000	Rosen et al. (2000)
$H_2O^+ + e^- \rightarrow OH + H$	$8.60 \times 10^{-8}\ (300/T_e)^{1/2}$	10–1000	Rosen et al. (2000)
$NH_3^+ + e^- \rightarrow NH_2 + H$	$1.55 \times 10^{-7}\ (300/T_e)^{1/2}$	10–300	Brian & Mitchell (1990)
$NH_3^+ + e^- \rightarrow NH + H + H$	$1.55 \times 10^{-7}\ (300/T_e)^{1/2}$	10–300	Brian & Mitchell (1990)
$H_3O^+ + e^- \rightarrow H_2O + H$	$7.09 \times 10^{-8}\ (300/T_e)^{1/2}$	10–1000	Novotný et al. (2010)
$NH_4^+ + e^- \rightarrow NH_2 + H_2$	$4.72 \times 10^{-8}\ (300/T_e)^{0.6}$	10–2000	Öjekull et al. (2004)
$NH_4^+ + e^- \rightarrow NH_2 + H + H$	$3.77 \times 10^{-8}\ (300/T_e)^{0.6}$	10–2000	Öjekull et al. (2004)
$NH_4^+ + e^- \rightarrow NH_3 + H$	$8.49 \times 10^{-7}\ (300/T_e)^{0.6}$	10–2000	Öjekull et al. (2004)
$H_3O^+ + e^- \rightarrow OH + H_2O$	$5.37 \times 10^{-8}\ (300/T_e)^{1/2}$	10–1000	Novotný et al. (2010)
$H_3O^+ + e^- \rightarrow OH + H + H$	$3.05 \times 10^{-7}\ (300/T_e)^{1/2}$	10–1000	Novotný et al. (2010)
$CO^+ + e^- \rightarrow O + C$	$2.00 \times 10^{-7}\ (300/T_e)^{1/2}$	10–1000	Mezei et al. (2015)
$HCNH^+ + e^- \rightarrow CN + H + H$	$9.30 \times 10^{-8}\ (300/T_e)^{0.65}$	10–300	Semaniak et al. (2001)
$HCNH^+ + e^- \rightarrow HCN + H$	$9.50 \times 10^{-8}\ (300/T_e)^{0.65}$	10–300	Semaniak et al. (2001)
$HCNH^+ + e^- \rightarrow HNC + H$	$9.50 \times 10^{-8}\ (300/T_e)^{0.65}$	10–300	Semaniak et al. (2001)
$H_3CO^+ + e^- \rightarrow CH_2 + OH$	$4.20 \times 10^{-8}\ (300/T_e)^{0.78}$	10–1000	Hamberg et al. (2007)
$H_3CO^+ + e^- \rightarrow CH + H_2O$	$1.40 \times 10^{-8}\ (300/T_e)^{0.78}$	10–1000	Hamberg et al. (2007)
$H_3CO^+ + e^- \rightarrow CO + H_2 + H$	$2.10 \times 10^{-7}\ (300/T_e)^{0.78}$	10–1000	Hamberg et al. (2007)
$H_3CO^+ + e^- \rightarrow H_2CO + H$	$2.17 \times 10^{-7}\ (300/T_e)^{0.78}$	10–1000	Hamberg et al. (2007)
$H_3CO^+ + e^- \rightarrow HCO + H + H$	$2.17 \times 10^{-7}\ (300/T_e)^{0.65}$	10–1000	Hamberg et al. (2007)
$CH_3OH_2^+ + e^- \rightarrow CH_2 + H_2O + H$	$1.87 \times 10^{-7}\ (300/T_e)^{0.59}$	10–300	Geppert et al. (2006)
$CH_3OH_2^+ + e^- \rightarrow CH_3 + H_2O$	$8.01 \times 10^{-8}\ (300/T_e)^{0.59}$	10–300	Geppert et al. (2006)
$CH_3OH_2^+ + e^- \rightarrow CH_3 + OH + H$	$4.54 \times 10^{-7}\ (300/T_e)^{0.59}$	10–300	Geppert et al. (2006)
$CH_3OH_2^+ + e^- \rightarrow CH_3OH + H$	$2.67 \times 10^{-8}\ (300/T_e)^{0.59}$	10–300	Geppert et al. (2006)
$CH_3OH_2^+ + e^- \rightarrow H_2CO + H_2 + H$	$8.90 \times 10^{-8}\ (300/T_e)^{0.59}$	10–300	Geppert et al. (2006)
$H_3S^+ + e^- \rightarrow H_2S + H$	$4.76 \times 10^{-8}\ (300/T_e)^{0.86}$	10–1000	Kamińska et al. (2008)
$H_3S^+ + e^- \rightarrow HS + H_2$	$4.20 \times 10^{-8}\ (300/T_e)^{0.86}$	10–1000	Kamińska et al. (2008)
$H_3S^+ + e^- \rightarrow HS + H + H$	$1.62 \times 10^{-7}\ (300/T_e)^{0.86}$	10–1000	Kamińska et al. (2008)
$H_3S^+ + e^- \rightarrow S + H_2 + H$	$2.80 \times 10^{-8}\ (300/T_e)^{0.86}$	10–1000	Kamińska et al. (2008)

provides the values for the electronic dissociative recombination kinetic coefficients used as a loss process for the total ion population in the ionospheric model in Section 2. Dissociative recombination is more significant at low cometocentric distances. Therefore, the recombination list used in the model does not involve every ion present in the model but only the ones that have a high number density close to the surface. Most of these rates are taken from UMIST data base (McElroy et al. 2013) and their accuracy lies within 25 per cent.

This paper has been typeset from a TEX/LATEX file prepared by the author.